Problems of Planetology, Cosmochemistry and Meteoritica

Barenbaum A.A. Key events of the Proterozoic eon: explanation using the galactic model. *UDC: 551.71/.72*

Oil and Gas Research Institе RAS. 119333. Moscow, Russia. *azary@mail.ru*

Abstract. The causes of the most important events of the Proterozoic eon are explained. These events include the formation of an oxygen atmosphere on Earth, the emergence of the Franceville biota and Ediacaran fauna, the onset of the Huronian and African ice ages, and the prolonged decline in Earth's geological activity between these events. Using a galactic model, it is established that these events at Proterozoic eon boundaries were caused by Sun's entry into the Crux-Scutum galactic arm, where Earth was subjected to more powerful and prolonged bombardments by galactic comets than in the other three galactic arms. At that time, comets bombarded the Earth's southern hemisphere, forming supercontinents on which powerful ice sheets developed. Comets also delivered large quantities of water and nutrients to Earth, facilitating the development of biota.

***Keywords**: Key events of the Proterozoic eon, galactic model, Galactocentric paradigm*

Introduction: Based on the galactic model (Barenbaum, 2022, 2022a), an explanation for several most important Proterozoic events, each of which has received its own name, is proposed. These events at the beginning of the Proterozoic included: the "oxygen revolution," which resulted in the emergence of an oxygen atmosphere on Earth; the "Lomagundi-Yatuli event," which resulted in the emergence of the Fransvillian biota; and the first glaciation on Earth – the "Huronian Glacioera." At the end of the Proterozoic, similar events included: the "African Glacioera," similar to the Huronian, which was accompanied by planetary glaciation according to the "Snowball Earth" hypothesis, and the emergence of the Ediacaran fauna in the Vendian. During the Middle Proterozoic, Earth's geological activity was much lower, and this period was dubbed the "Boring Billion" and the "Great Glacial Pause." These facts, their discussion and explanation are given below.

Facts: Fig. 1 shows the change in the partial pressure of oxygen in the oxygenic photosynthesis atmosphere (Lyons et al., 2014). In the Archean (up to 2.5 billion years ago), the O_2 content in the atmosphere was ~10^{-6} of today's levels. At the Archean-Archean boundary ~2.3 billion years ago, PO_2 suddenly reached today's values, but ~2.1 billion years ago, it dropped just as sharply. This event has been given various names, such as the "oxygen revolution," the "great oxygen event," the "oxygen crisis," and the "oxygen catastrophe." But the general conclusion was that oxygen on Earth was produced by cyanobacteria.

At the end of Proterozoic, at the boundary with the Phanerozoic, in the Vendian period, atmospheric oxygen levels again increased sharply, triggering another extraordinary event, known as the "Vendian-Cambrian explosion of life." During this period, the soft-bodied "Ediacaran fauna" emerged, becoming extinct by the end of the Vendian, and in the Cambrian was replaced by modern species of life, followed by plants. All these changes are now explained by the increase in atmospheric O_2 levels.

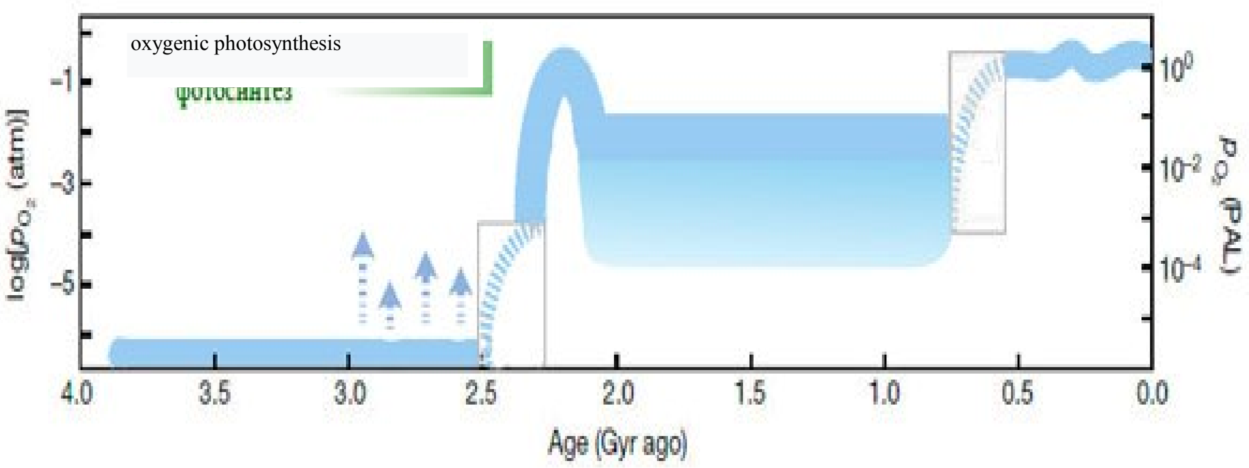

Fig. 1: Partial pressure of oxygen in the atmosphere PO_2 on Earth according to (Lyons et al., 2014). The right axis is relative to the modern level, the left axis is the common logarithm. Arrows indicate possible O_2 "emissions" at the end of the Archean. Rectangles represent PO_2 changes during the transition from the late Archean to the early Proterozoic and from the late Proterozoic to the early Phanerozoic.

Figure 2 shows data from isotopic studies (Lyons et al., 2014). These data indicate that, at the PO_2 maximum of ~2.3 billion years ago, large amounts of carbon enriched in the $\delta^{13}C$ isotope were deposited on Earth. Meanwhile, at ~2.1 billion years ago, when the O_2 content dropped sharply, black shales with a deep negative $\delta^{13}C$ carbon excursion were deposited.

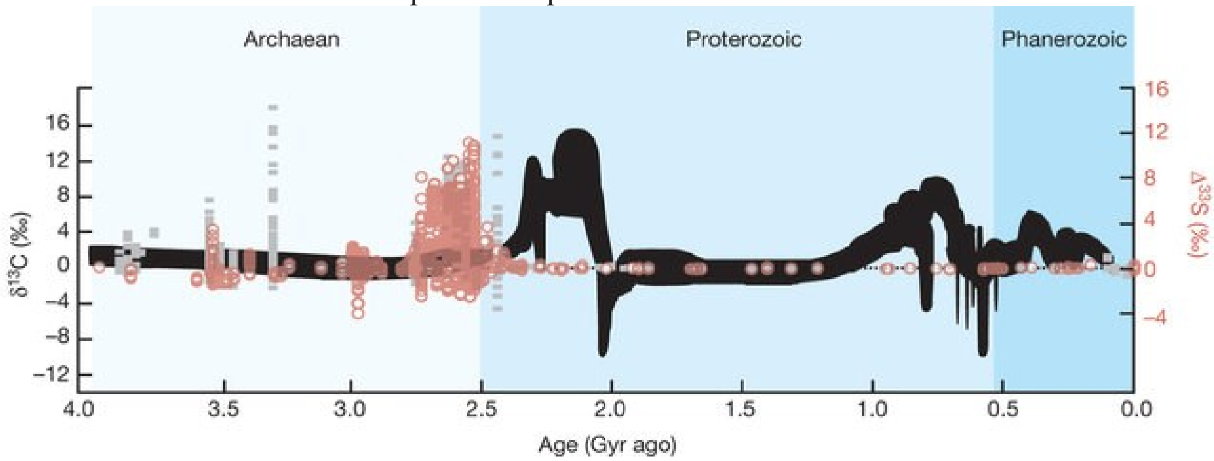

Fig. 2: Summary of carbon (black) and sulfur (red and gray) isotope data in Earth's history (Lyons et al., 2014). Data are presented as $\delta^{13}C$ (left axis) and $\Delta^{33}S = \delta^{33}S - 0.515\delta^{34}S$ (right axis).

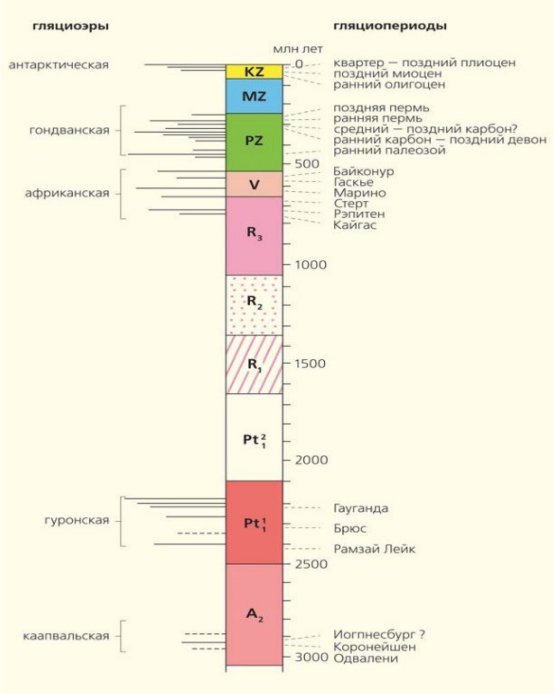

Fig. 3. Glacioeras and glacioperiods on Earth according to N.M. Chumakov (2015)

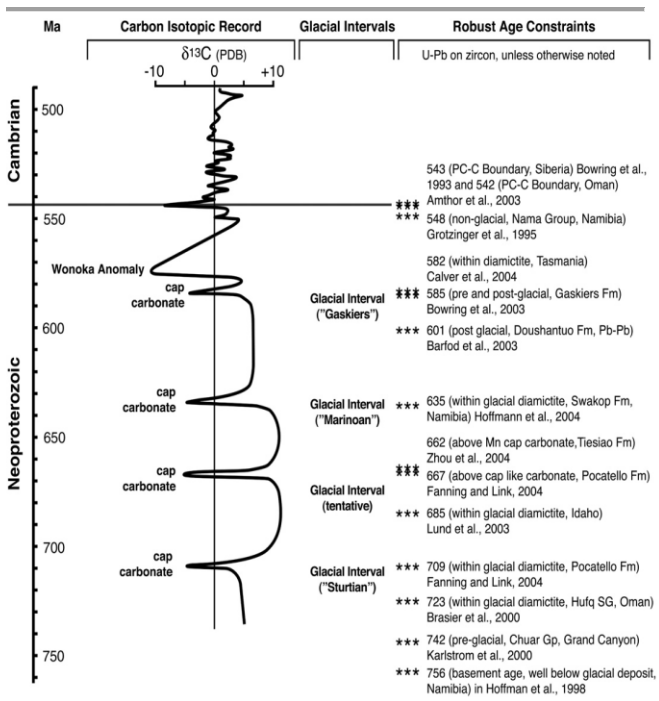

Fig. 4. Simplified summary of δ13C measurements in carbonates (Hebert C.L. et al., 2010)

Both processes are known as the "Lomagundi-Yatuli events" (after the region where they were first discovered). The event itself was planetary in nature, and similar $\delta^{13}C$ isotopic anomalies have been found in numerous sedimentary deposits of the same age across the globe.

During the Lomagundi-Yatul event, the "Franceville biota" emerged on Earth. This biota consisted of multicellular organisms several centimeters in size that inhabited oxygen-rich aquatic environments and performed aerobic respiration (El Albani, 2014). Following this event, these organisms disappeared immediately. It is worth noting that in many respects, the Franseville biota is similar to the Ediacaran fauna, which arose in the Vendian and became extinct at its end at the Proterozoic-Phanerozoic boundary.

For completeness, we note that the PO_2 surges at the beginning and end of the Proterozoic (Fig. 1) and the accompanying $\delta^{13}C$ isotopic anomalies (Fig. 2) coincide with the development of planetary glaciations on Earth—the Huronian and African

Glacioeras (Fig. 3). Fig. 4 shows detailed δ13C variations in carbonates (Hebert et al., 2010) during the African Glacioera (720–570 million years ago). No glaciations were observed between the two Glacioeras, leading to the term “Great Glacial Pause.” During this period, the oxygen level (Fig. 1), although it changed, was on average low. The climate also did not change significantly, and the evolution of living organisms on our planet was relatively slow. This is why the Middle Proterozoic has been called the “boring billion,” the “desert billion,” and the “barren billion.”

During the African Glacioera (Fig. 4), the continents were cyclically covered by powerful ice sheets, the melting of which deposited $CaCO_3$ and $CaMg(CO_3)_2$ carbonates characterized by positive $\delta^{13}C$ anomalies. Whereas during times of relatively short cometary bombardments, carbonates with sharply negative $\delta^{13}C$ deviations were formed. According to the “Snowball Earth” hypothesis, glaciers could have covered all continents of our planet during the African Glacioera.

Discussion

The author explains these facts in his works (see bibliography) based on the Galactocentric paradigm concept, which, using the galactic model, allows to study the early stages of the geological development of the Earth under the conditions of cyclic bombardments of the Solar System by galactic comets. Therefore, we will briefly review the Galactocentric paradigm concept and the galactic model.

The Galactocentric paradigm concept assumes:

The Sun and planets formed 6.567 billion years ago, and the event 4.567 billion years ago marks the beginning of the second major stage of their formation, caused by the destruction of the planet Phaeton and the formation of the modern asteroid belt in its place. During the initial, most active stage of Phaeton's fragmentation, its large fragments fell in large numbers onto all the planets closest to the belt, including Earth.

At the time of Phaeton's destruction, Earth was already formed planet. It had an anorthositic crust, an iron-nickel core, and mantle shells similar to modern ones, but with a higher iron content in the silicates. As a result of the falls of large Phaeton debris, our planet lost approximately 245-kilometer-thick layer of surface rock, which consisted of one-third primary anorthositic crust and two-thirds mantle rocks. Some of these rocks formed the Moon, some were lost, and some fell back to Earth, mixed with its material, melted, and turned into a “magma ocean” approximately 100 km deep.

The resulting “magma ocean” began to cool very rapidly under the influence of falling galactic comets. Simultaneously, a solid surface emerged on Earth, where water brought by galactic comets began to accumulate, and the World Ocean began to form. As a result, at the Archean (4.0–2.5 billion years ago), Earth already had vast water basins and an oxygen-free atmosphere. However, surface temperatures were still very high, making Earth unsuitable for life.

The galactic model calculates the periods of galactic comet falls of varying intensity, allowing for the construction of unified, highly accurate geochronological scale for the Phanerozoic and Precambrian, as well as answering other questions about Earth's early geological development. The model establishes:

The Sun formed 6.567 billion years ago in the Crux-Scutum spiral arm and has since moved in the Galaxy plane along a slowly rotating elliptical orbit in resonance with the rotation of the four spiral arms and the Galaxy's nuclear disk, from which two jet streams flow. The rotation period of the Sun orbit's apsidal line (the Molchanov resonance period) is 2.0 billion years.

During its orbital motion, the Sun crosses spiral arms and jet streams, and during these periods, Earth is subjected to intense bombardment by galactic comets, which are the primary cause of planetary tectonomagmatic, climatic, and biotic processes on Earth. Comets cyclically deliver water and other cosmic substances to Earth, which are incorporated into the global geochemical cycle of matter and participate in the formation of many mineral resources.

The model showed: 1) The Crux-Scutum arm is “wider” and cometary bombardments in it is much more powerful than in the other three Galaxy arms. 2) Key events in Earth's history, associated with its formation and the emergence of the Moon, as well as at the highest stratigraphic boundaries of the Eonothem rank — Archean-Proterozoic and Proterozoic-Phanerozoic — occurred in this arm and repeated with a strict period of 2 billion years. 3) The ecliptic plane of the Solar System, along which the planets revolve around the Sun, also precesses with this period, which plays an important role in the cyclical formation and disintegration of supercontinents.

Conclusion

The key events of the Proterozoic that led to the formation of Earth's modern oxygen atmosphere at the Cambrian-Proterozoic and Proterozoic-Phanerozoic boundaries, as well as the emergence of highly developed living beings at these boundaries, are explained by two main factors: 1) by high temperatures on Earth after the Moon formation and their subsequent decrease in the processes of cooling of the resulting “magma ocean”, 2) powerful and prolonged bombardments of Earth by galactic comets in the Crux-Scutum arm at the beginning and end of Proterozoic, which caused a significant decrease in temperatures.

In both cases, galactic comets bombarded the Earth's Southern Hemisphere, bringing with them enormous quantities of water. Cometary impacts may have cooled the planet's surface so much that ice caps formed on the continents of the Southern Hemisphere, where supercontinents were forming at the time. At the beginning of the Proterozoic, the supercontinent Kenorland was located here, and at the end of the Proterozoic, the supercontinent Pannotia. Between comet bombardments in Crux-Scutum arm Earth's temperature increased, and glaciations did not occur.

Thus, Earth's oxygen-rich atmosphere was formed by the falls of galactic comets, not by living organisms. Life is a cosmic phenomenon. Its lower prokaryotic forms present on Earth since its formation, whereas in space they always exist. With the appearance of liquid water on Earth's surface and decreasing temperatures, life in aquatic environments rapidly evolved.

Thus, Earth's oxygen-rich atmosphere was formed by the falls of galactic comets, not by living organisms. Life always exists in space, and its lower forms—prokaryotes— present on Earth since its formation. With the appearance of liquid water on Earth's surface and a drop in temperature, prokaryotes in aquatic environments rapidly evolved. During periods of cometary bombardments in the Crux-Scutum arm, at the beginning of the Proterozoic, the Francevillian biota emerged, at the end of the Proterozoic, the more advanced Ediacaran fauna appeared. In the Phanerozoic, when Earth's temperature conditions became more favorable, living organisms populated not only the ocean but also land.

References

Barenbaum A.A. The Galactocentric Paradigm in Geology and Astronomy – M.: LIBROKOM, 2010, 546 p.

Barenbaum A.A. The cause of the "biotic revolution" in the Vendian-Cambrian from the standpoint of the comet-galactic hypothesis // Doklady AN, 2004, Vol. 398, No.4, 513–515.

Barenbaum A.A. Confirmation of the "Snowball Earth" hypothesis by the galactic model // Geology of the Seas and Oceans. 2021. Moscow: Institute of Oceanology RAS, 21–25.

Barenbaum A.A. Analysis of the causes of glaciations and $\delta^{13}C$ anomalies in carbonates based on the galactic model // Physicochemical and Petrophysical Studies in Earth Sciences. Conference Proceedings. – Moscow: IGEM RAS. 2021, 22–26.

Barenbaum A.A. Bombardments of Earth by galactic comets and supercontinental cyclicity // Experiment in Geosciences. 2022, Vol.28, No1, P. 8–13.

Barenbaum A.A. Measuring the precession period of Solar System ecliptic plane using galactic model // The 13 Moscow Solar System Symposium, October 10-14, 2022, Book of abstracts. Moscow: Space Research Inst. RAS, 2022, Poster 13MS3-GP-PS-04.

Barenbaum A.A. Solution of problem questions of astronomy and geology using the optimized galactic model // Book: Physical and Mathematical Modeling of Earth and Environment Processes. V.E. Karev (Ed.), 2022. DOI: 10.1007/978-3-031-25962-3.

Barenbaum A.A. On the issue of "True polar wander" phenomenon and its alternative physical interpretation based on galactic model // Processes in GeoMedia—Volume VII., 2023, 49-69. DOI: 10.1007/978-981-99-6575-5.

Barenbaum AA. Cosmogony of Open Solar System (I): Formation of giant planets and origin of the Moon // Processes in GeoMedia—Volume IX. Springer Nature Link, 2025, 31–64. DOI:10.1007/978-981-96-9302-3_3

Barenbaum AA. Cosmogony of Open Solar System (II): Model of secondary planet formation, secondary accretion disk of the Sun, formation of satellites of giant planets, Molchanov's resonance, Titius-Bode rule // Processes in GeoMedia—Volume IX. Springer Nature Link, 2025, 65–107.

Barenbaum A.A., Gladenkov Yu.B., Yasamanov N.A. Geochronological scales and astronomical time // Stratigraphy. Geological correlation. 2002. Vol. 10, No. 2, 3–14.

Barenbaum A.A., Litvinova T.V., Khain V.E. Geological evidence of the influence of space on the evolution of life. The Vendian-Cambrian biotic event // Ural Geological Journal. 2009, No.6 (72), P. 15–39.

Barenbaum A.A., Yasamanov N.A. On a possible cause of sheet glaciations // Bulletin of the Moscow Naturalists. Department of Geology, 2004, Vol.79, Is. 6, 13-21.

Chumakov N.M. Glaciations of the Earth: History, Stratigraphic Significance and Role in the Biosphere. Moscow: GEOS, 2015, 160 p.

El Albani A. at al. The 2.1 Ga Old Francevillian Biota: Biogenicity, Taphonomy and Biodiversity. 2014, PLoS ONE 9(6): e99438. https://doi.org/10.1371/journal.pone.0099438

Lyons T.W., Reinhard C.T., Planavsky N.J. The rise of oxygen in Earth's early ocean and atmosphere // Nature, 2014, Vol. 506, Is.7488, 307-315.

Hebert C.L. et al. Radiometric and stratigraphic constraints on terminal Ediacaran (post-Gaskiers) glaciation and metazoan evolution // Precambrian Research. 2010, Vol.182, 402–412.

Basilevsky A.T.[1], Head J.W.[2] On the problem of determination of the composition of material comprising Venus surface geologic-morphologic units. *UDC 523.42*

[1]GEOKHI RAN, Moscow, Russia atbas@geokhi.ru, [2]Brown University, Providence, USA James_Head@Brown.edu

Abstract. Surface materials in the landing sites of Venera-8, 9, 10, 13, 14 and Vega-1 and 2 could be composed of ejecta from impact craters, located in other parts of Venus, and deposited from the atmosphere as radar-dark parabolas generated by the impacts. This raises the question if whether the lithified surface material observed in these places represents in-situ geologic-morphologic units in these localities or instead partly or completely represents ejecta from distant craters. In either case, in future missions aiming to measure the composition of local bedrock, it would be reasonable to avoid the possible influence of observed and modeled radar-dark parabolas, and to increase the certainty of sampling local bedrock, to drill down to the depth of a few meters.

***Keywords**: Venus, landing site, rock composition, radar-dark parabola*

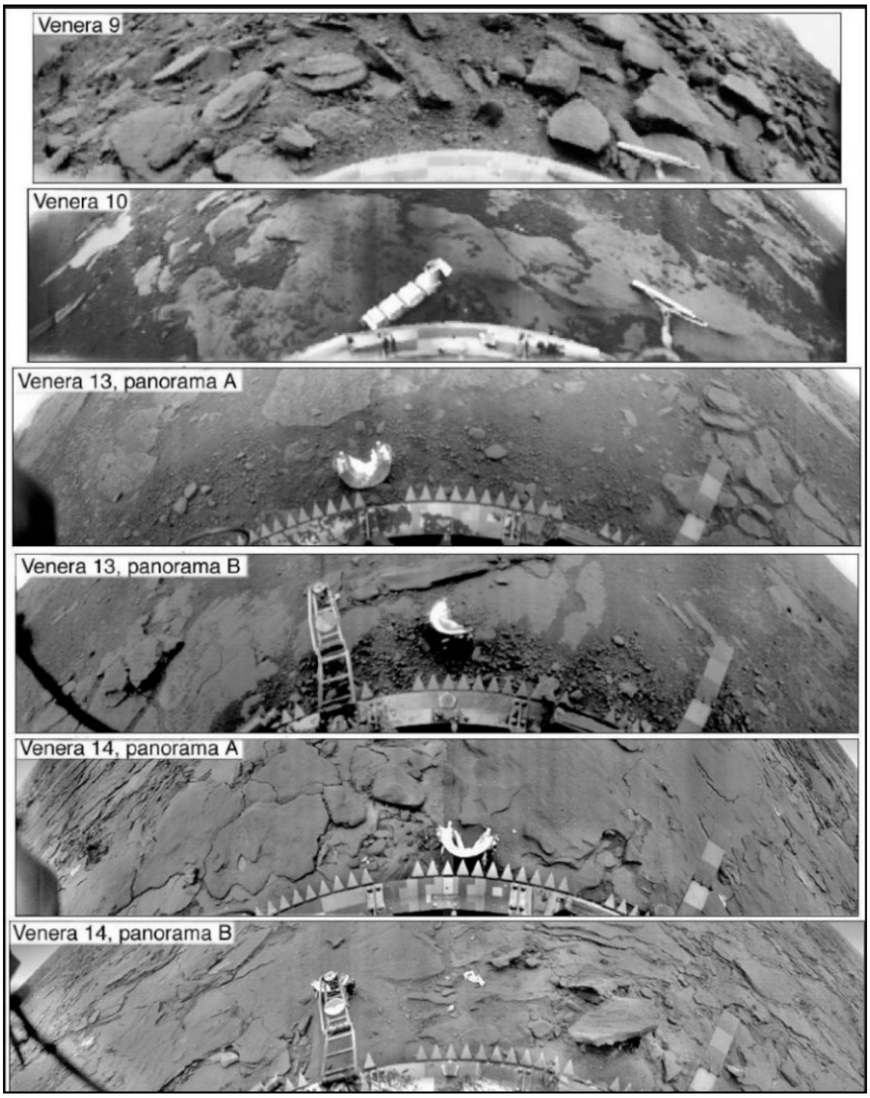

Fig. 1. TV panoramas in the landing sites of Venera-9, 10, 13 and 14. The TV camera is at a height 1 m above the surface and inclined forward. T-shape feature in the right portion of Venera-9 and 10 panoramas is the gamma-densitometer. The length of its transverse part is 40 cm. The light segmented feature in the center of the Venera-10 panorama is the ejected cap covering the TV camera during descent. Its size is 10 x 40 cm. Arc-like features (~20 cm in diameter) in the center of the Venera-13 and 14 panoramas are ejected TV camera caps. In the right part of the Venera-13 and 14 panoramas are seen photometric standards as long as 40 cm. In the central part of Venera-13B and Venera-14B panoramas is seen the 60-cm long trellis girder with the penetrometer to determine strength of the surface material. On the landing rings of Venera-13 and 14 are seen teeth. The distance between their ends is 5 cm. Knowledge of these scales allows to determine sizes of surface features: thickness of the layers, sizes of rock fragments and etc.

Venus is a critically important terrestrial planet to compare to Earth and Venus-like exoplanets (Ostberg et al., 2023) and in the next decade armada of missions are planned to be sent by Russia, India, ESA, China and the United States. Included among the armada will be missions aiming to measure the compositions of the geologic-morphologic units of the Venus surface. In 1970-80 the Soviet automatic stations Venera-8, 9, 10, 13, 14 and Vega-1 and 2 measured the compositions of surface materials in the landing sites and the measurement results were correlated with geologic-morphologic units, identified in analysis of the images obtained by side-looking radar of Magellan spacecraft (e.g., Basilevsky et al., 2007; Ivanov and Head, 2011). However, based on analysis of TV panoramas of the surface in the landing sites of Venera-9, 10, 13 and 14 (Fig.1) (Basilevsky et al., 2004) and data on the strength of the surface materials (Kemurdzhian et al., 1983), it was shown that the finely (centimeters) layered rocks observed in panoramas probably could be the lithified fine-grained deposits of ejecta from distant impact craters larger than 11 km in diameter that form radar-dark parabolas (Fig. 2).

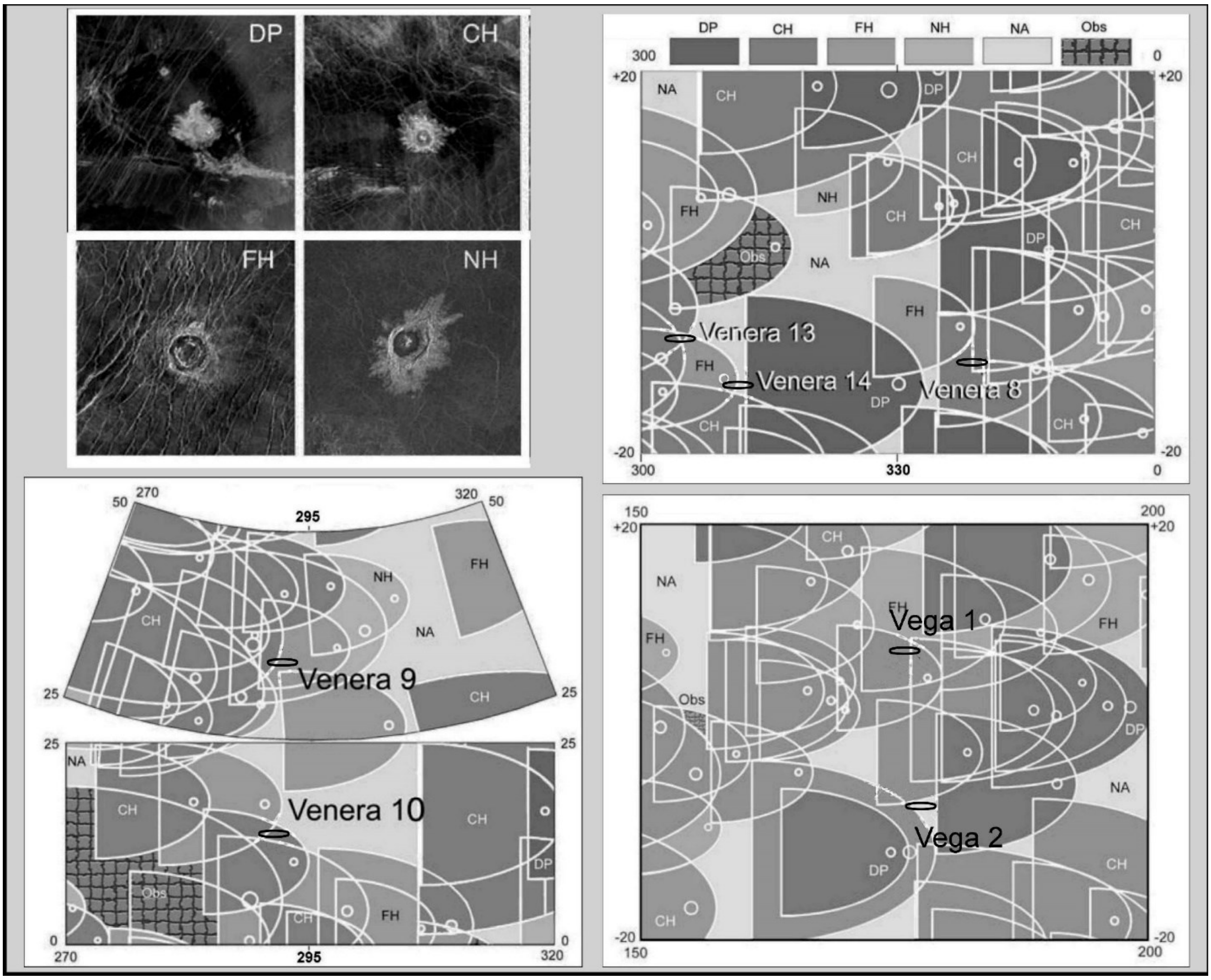

Fig. 2. Upper left: Examples of radar-dark parabola (DP) and stages of its degradation into clear halo (CH), faint halo (FH) and absence of halo (NH). Upper right and lower left and right: Maps of the observed (DH) and model (CH, FH, NH) parabolas associated with craters. *Obs* means that vicinity of this crater is covered by other deposits so it is impossible to classify the model parabola of this crater. *Black ellipses* in the maps near the spacecraft names are the landing ellipses 350 x 50 km (Basilevsky and Head, 2026).

In panoramas presented in Figure 1, in their central parts is seen terrain near the spacecraft, while on the left and right sides, – distant areas up to local horizon are observed. Close to the spacecraft are seen outcrops and fragments of finely layered rocks and between them, finely-grained darker soil. The fragments are from a few to several tens of centimeters across. Based on the magnitude of overload at the landing event the surface material strength was estimated to be 4-5 kg/cm^2, suggesting a porosity of 50-60% (Avduevskiy et al., 1983). Measurements by penetrometer at the Venera-13 landing site showed values of 2,6-10 kg/cm^2 (Kemurdzhian et al.,1983). It is observed in Fig. 1 that the penetrometer of Venera-14 impacted the illuminator cap so strength of the surface material was not measured. The material surface strength was also estimated from the telemetry data obtained during the drilling to take samples for X-ray-fluorescence analysis at Venera-13 and 14. The resistance was analogous to that at drilling weathered porous basalt or tuff (Barmin and Shevchenko, 1983). Basilevsky at al. (2004) concluded that the finely layered low-strength rocks observed in the panoramas are lithified deposits of fine-grained fraction of ejecta from impact craters, located in other places, deposited from the atmosphere and observed as radar-dark parabolas (Fig. 2).

Figure 2 shows that the landing ellipses are covered by one-two-three parabolas so the surface material there is more likely not local but transported from the distant crater that is the source of the parabola. In addition, because the parabola material is comprised of the fine fraction of the crater ejecta cloud blown to the west by typical Venus longitudinal winds, this material is at some degree represents the planetary crust penetrated by these craters, but not the local, in-situ geologic-morphologic unit at the landing site. To predict where there is high probability of sampling only the in-situ surface the material representing the local geologic-morphologic unit, in Fig. 3 we superposed the map of the observed and modeled parabolas taken from Ganey et al. (2023) onto the geologic map by Ivanov and Head (2011).

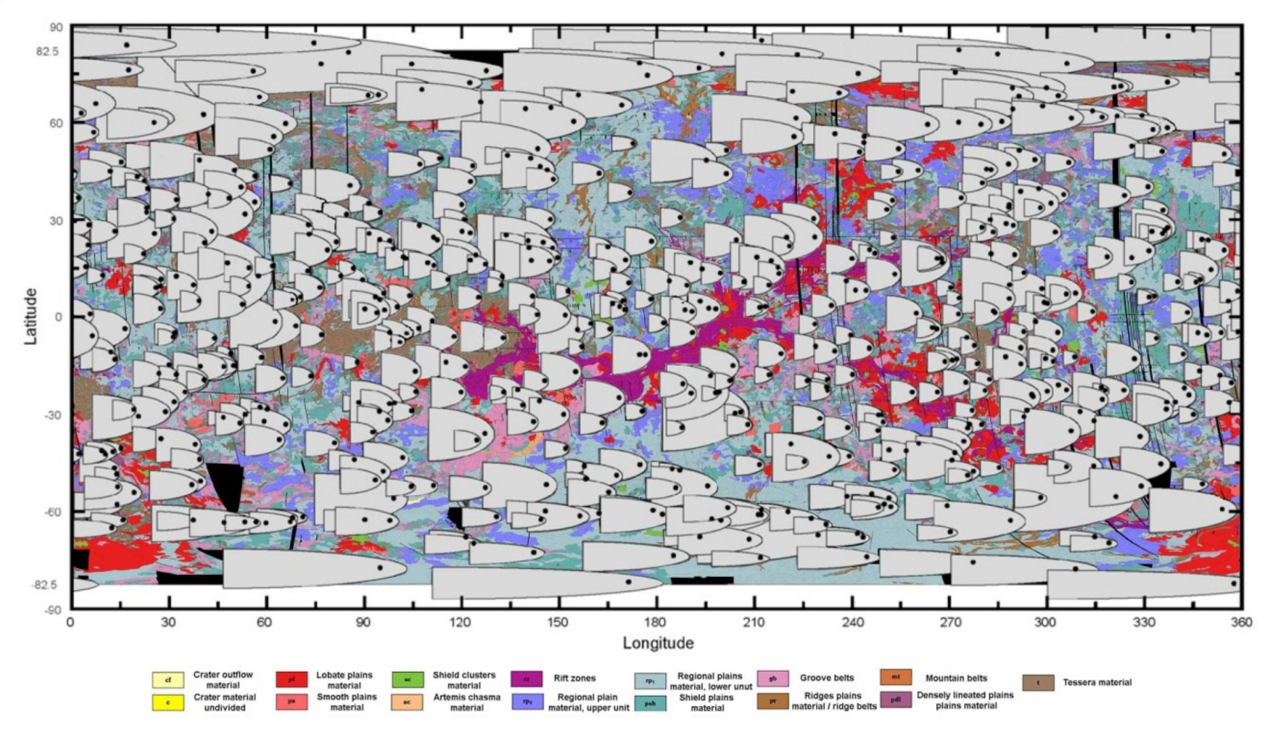

Fig. 3. Geologic map of Venus (Ivanov and Head, 2011) with superposed parabolas (Ganey et al., 2023)**.**

On the basis of Fig. 3, it is clear that surface of Venus is covered by numerous observed and modeled parabolas. But this is not complete global coverage and, in many places, there are rather large areas that may not contain parabola material on the surface. Of course, these are models and the parabola material can be outside the boundaries of the mapped parabolas. Nevertheless, we believe that the map shown in Fig. 3 can be used to assist in selecting landing sites for the missions in which measurements of composition of these and those geologic units are planned. And to decrease the risk of measuring only parabola compositions, and not that of the in-situ geological units, it is necessary to drill down to several meters.

Funding. The work was carried out by A.T. Basilevsky using budget funding from the Vernadsky Institute of Geochemistry and Analytical Chemistry, Russian Academy of Sciences.

Acknowledgments*. Authors are grateful to those who made the side-looking radar for the Magellan spacecraft, produced TV cameras for the Venera-9, 10, 13 and 14 landers, and measured strength of the surface material in the landing sites.*

References

1. Avduevsky V. S. et al., An estimate of the physical and mechanical characteristics of the soil of Venus from measurements of the impact overload during the landing of the Venera 13 and Venera 14 automatic interplanetary stations (in Russian), Kosm. Issled., 1983, 21, 331– 339.
2. Barmin, I. V. and Shevchenko A. A., Soil-scooping mechanism for the Venera 13 and Venera 14 unmanned interplanetary spacecraft (in Russian), Kosm. Issled., 1983, 21, 171– 175.
3. Basilevsky A. T. and Head J. W. On the problem of composition of material of geologic-morphologic units of Venus. Solar System Research. 2026 (in press).
4. Basilevsky A.T., Ivanov M.A., Head J.W., Aittola M. and Raitala J., Landing on Venus: Past and future. Planetary and Space Science, 2007, 55(14), 2097-2112.
5. Basilevsky A. T., Head J. W., Abdrakhimov A. M. Impact crater air fall deposits on the surface of Venus: Areal distribution, estimated thickness, recognition in surface panoramas, and implications for provenance of sampled surface materials. JGR, 2004, 109, E12003, 18 p.
6. Ganey TM., Gilmore M.S., Brossier J. Reassessment of the volumes of sediment sources and sinks on Venus. The Planet. Sci. J., 2023, V. 4, No 9, 20 p.

7. Ivanov M.A. and Head J.W. Global geologic map of Venus. Planetary and Space Science. 2011, 59(13), 1559-1600.
8. Kemurdzhian A. L., et al., Preliminary results of determining the physical and mechanical properties of the soil of Venus by the Soviet automatic stations Venera 13 and Venera 14 (in Russian), Kosm. Issled., 1983, 21, 323– 330.
9. Ostberg C., Kane S.R., Li Z., Schwieterman F.W., Hill M.L., Bott K., Dalba P.A., Fetherolf T., Head J.W. and Unterborn C.T. The demographics of terrestrial planet in the Venus zone. The Astronomical Journal. 2023. 165 (4), p. 168.

Guseva E.N. and Ivanov M.A. Results of morphometric analysis of the Venus coronae. *UDC 523.42*

Vernadsky institute of RAS, 119991, Moscow, Russia, guseva@geokhi.ru, ivanov.m@geokhi.ru

Abstract. We analyzed the morphometric and topographic features of the Venus coronae and found that: (1) the majority of the coronae (~ 83%) are topographically mature pre-rift structures and only a small part of coronae (~ 17%) are young rift-related features; (2) the mature pre-rift coronae are less volcanically active compared with the younger, dome-shaped, coronae; (3) the topographic amplitude of the rift-related coronae is about two times larger compared with the older coronae; (4) at the final stages of evolution of coronae, when they gain the shape of simple depressions (the topographical class U), the both the amplitude of vertical relief and average diameter of the rift-related coronae are about two times larger than those parameters of the older coronae. All these differences probably arise because the older coronae likely formed in the conditions of thinner lithosphere. When the rift coronae formed, the lithosphere became thicker due to vertical accretion during the late Atlian period.

***Keywords**: Venus, coronae, morphometry, topography, volcanism, rifting, stages of coronae evolution*

Coronae are large concentric structures, ranging in diameter from 75 to 2,500 km, first discovered on the surface of Venus by the Venera 15 and 16 missions (Barsukov et al., 1984; Crumpler and Aubele, 2000). Hundreds of coronae are widely distributed over the planet's surface and are identified by a characteristic feature of annulus (topographic ridge) consisting of closely spaced grooves and/or ridges (Barsukov et al., 1986; Pronin and Stofan, 1990). Volcanic formations predominate in the inner part of the coronae (Stofan et al., 1992).

Coronae are thought to be the surface manifestation of mantle diapirs (Nikishin, 1990; Pronin and Stofan, 1990; Stofan et al., 1992; Koch and Manga, 1996; Smrekar and Stofan, 1997), whose dimensions determine the size of coronae (Kreslavsky and Vdovichenko, 1996). The characteristic topographic profiles of coronae vary and reflect different phases of diapir evolution (Smrekar and Stofan, 1997). Coronae profiles are changed from a dome-shaped uplift (class D) at the progressive stage of diapir evolution to topographically complex (class W) and then simple (class U) depressions at the regressive stages (Guseva and Ivanov, 2022). During the progressive stage, the diapir presumably stops at the base of the lithosphere and bends it upward due to positive buoyancy. During the regressive stage, the diapir apparently acquires negative buoyancy due to heat loss and subsides (Guseva and Ivanov, 2024).

Coronae formed predominantly during the ancient Guinevrian and partially during the younger Atlian periods of Venus's geologic history (Basilevsky and Head, 1995; 2000; Ivanov and Head, 2011). Their volcanic activity faded away primarily during the pre-Atlian period (Basilevsky and Head, 1995; 2000; Ivanov and Head, 2011). Only a small part of coronae (~ 17%) exhibit volcanism in the form of flows of lobate plains during the Atlian period (Guseva and Ivanov, 2023). The most common sources of corona volcanism are extensional structures of the coronae annulus and/or swarms of radial grabens propagating from some specific centers (not always corresponding to the center of a corona). Less commonly, the eruption sources within a corona have no morphological manifestations.

The typical spatial associations of coronae with regional extensional zones of groove belts and rifts may indicate their genetic relationship (Stofan et al., 1997).

The goals of this study were to determine how the morphometric characteristics of coronae vary depending on the evolutionary stage and age of the annulus and what factors may be associated with these changes.

Morphological and topographic characteristics of coronae

Two main morphological types of annulus characterize coronae: those composed of the older groove belts (pre-rift) and annulae consisting of the young rift zones (rift) (Guseva and Ivanov, 2019).

The pre-rift coronae are characterized by their much broader areal distribution on the surface of Venus. In contrast, the rift coronae are tightly associated with rift zones that have limited extent (fig.1).

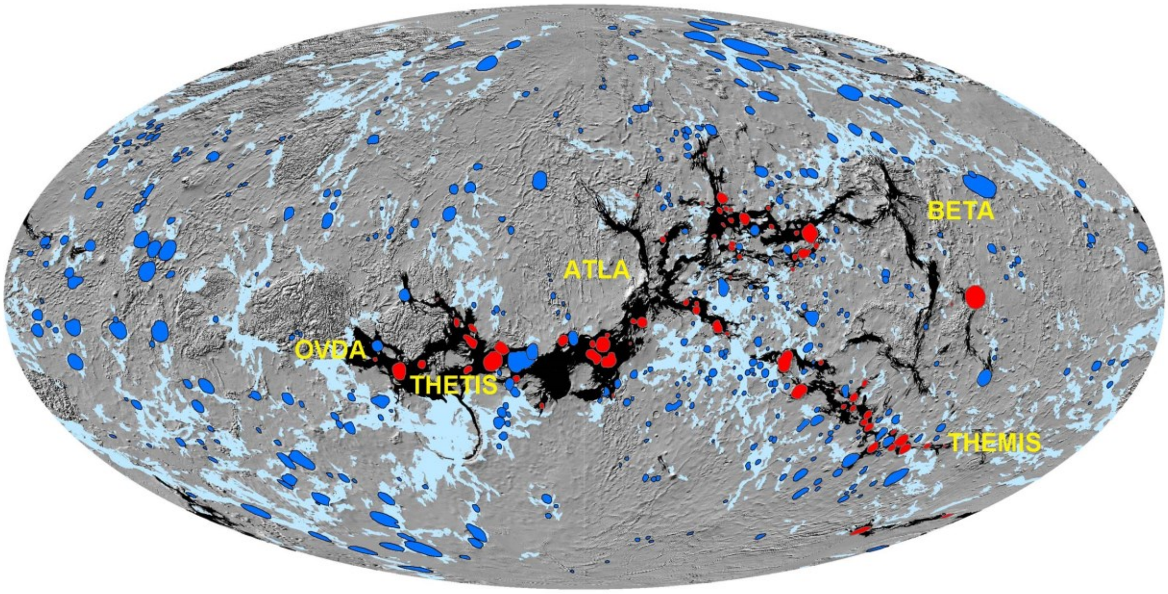

Fig. 1. Distribution of coronae on the surface of Venus and their relationships to regional extension zones: the pre-rift coronae (blue) and the rift coronae (red). Groove belts (gb) are shown in blue, rift zones (rz) are in black. Geological boundaries are from Ivanov, Head (2011). The map is in the Mollweide equal-area projection, central meridian 180°.

Pre-rift coronae constitute the majority of the studied population ~ 83% (330 of 397 coronae). These are primarily coronae with annulus of groove belts (253 of 330 coronae, gb, fig. 2a). Less commonly, these are coronae without a distinct morphological annulus, or partially or completely embayed by regional and/or lobate plains (50 of 330 coronae). In rare cases, these are coronae with annulus of ancient groove belts deformed by young rift fractures (27 of 330 coronae). The U and W topographic classes (148 and 139 of 330 coronae) are dominated among the pre-rift. The D topographic class characterizes a small fraction of these coronae (43 coronae, fig. 3, table 1). Only a small part of the pre-rift coronae (~ 15%, 51 coronae) represent distinct volcanic sources.

Rift coronae (fig. 2b) constitute ~ 17% of the studied population (67 coronae). Topographically, they are represented mainly by D-class structures (30 of 67 coronae), and less frequently by the W- and U-classes (20 and 17 coronae, fig. 3, table 1). About half of the rift coronae are volcanic sources (~ 46%, 31 coronae).

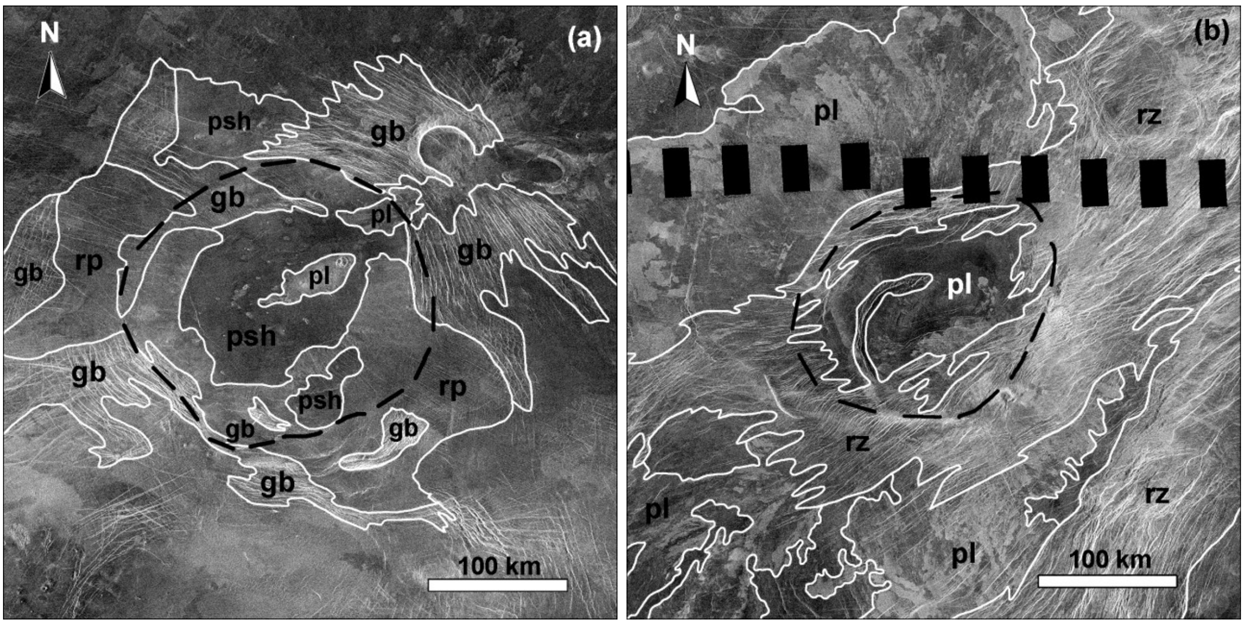

Fig. 2. (a) The pre-rift, Durga Corona, topographic class U; (b) the rift corona, Nahas-tsan Mons, topographic class D. White lines are boundaries of groove belts (gb), rifts (rz), shield plains (psh), regional plains (rp), lobate plains (pl); the annulae of coronae are shown with a black dashed line.

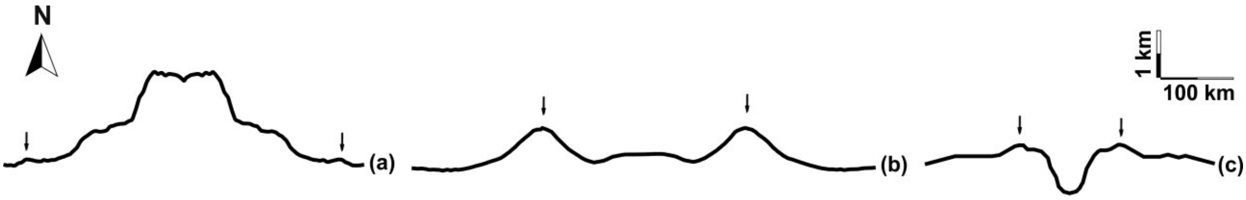

Fig. 3. Examples of topographic profiles of coronae: (a) D-class, domed uplift, progressive stage of the parent diapir evolution; (b) W-class, complex depressions, regressive stage of the parent diapir evolution; (c) U-class, simple depressions, final stage of the parent diapir evolution. Arrows show the annulus of the coronae.

Morphometric features of coronae depending on the stages of their evolution

Pre-rift coronae are preferentially the topographically mature structures reflecting the regressive stages of the parent diapir evolution. Only in rare cases, these coronae are characterized by structures (e.g., a central dome) that may correspond to the progressive stage of evolution. Coronae that are represented in the topography by complex and simple depressions of the W and U topographic classes compose ~ 87% of the population (287 of 330 coronae, table 1). The pre-rift coronae with the domed uplifts of the D topographic class make up about 13% of the population (43 of 330 coronae). The domed coronae can exhibit volcanic activity (18 of 43 coronae, 42% of the population of pre-rift coronae of D class). In general, only 15% (51 of 330 coronae) of all pre-rift coronae are characterized by the presence of volcanic activity. The average diameter of pre-rift coronae varies within the range of 168±50 km to 242±73 km, the amplitude of vertical relief – within the range of 0.7±0.2 km to 1.2±0.2 km.

Rift coronae are both topographically mature and immature structures reflecting the regressive and progressive stages of evolution of the parent diapirs. Coronae, represented topographically by complex and simple depressions of classes W and U, constitute approximately 55% of the entire population (37 of 67 coronae, table 1). The domed coronae of class D constitute approximately 45% of the population (30 of 67 coronae). The rift coronae are characterized by the following average diameters and vertical relief amplitudes: ~ 226±66 km and 1.8±0.4 km, respectively. Thus, the rift coronae are comparable to the pre-rift coronae by their average diameter but their vertical relief amplitude is about twice as large.

Table 1. Morphometric and topographic characteristics of the Venus coronae

Morphological type of coronae	Total coronae, units, %	Topo-class, total coronae	Of these, sources of volcanism, units, %	Diameter, average, km	Amplitude of vertical relief, average, km
Pre-rift coronae	330 (83)	D (43)	18 (42)	242±73	1.2±0.2
		W (139)	17 (12)	218±65	0.8±0.2
		U (148)	16 (11)	168±50	0.7±0.2
Rift coronae	67 (17)	D (30)	21 (70)	205±61	2.2±0.4
		W (20)	5 (25)	204±61	1.5±0.4
		U (17)	5 (29)	287±80	1.5±0.4

We analyzed how the morphometric features of coronae change within each topographic class.

Dome-shaped coronae of class D. The pre-rift coronae: 43 coronae total, of which 18 are volcanically active, their average diameter is ~ 242±73 km, the average amplitude of the vertical relief is ~ 1.2±0.2 km (table 1). The rift coronae: 30 coronae total, of which 21 are volcanically active, their average diameter is estimated at ~ 205±61 km, the average amplitude of the vertical relief is ~ 2.2±0.4 km. Thus, the dome-shaped coronae with the annulus of different morphological types are comparable in diameter, but differ significantly in the amplitude of the vertical relief. The rift coronae of D class are more often characterized by volcanic activity (21 of 30 coronae, ~ 70%) in contrast to the pre-rift coronae (18 of 43 coronae, ~ 42%).

Class W, complex depressions. The pre-rift coronae: 139 coronae total, 17 of them show signs of volcanic activity, their average diameter is ~ 218±65 km, and the average vertical relief amplitude of is ~ 0.8±0.2 km (table 1). The rift coronae: 20 coronae total, 5 of which show signs of volcanism, their average diameter is ~ 204±61 km, and the average vertical relief amplitude is ~ 1.5±0.4 km. The coronae of the W topographic class with annulus of different morphological types are also comparable in diameter, but differ approximately twice in vertical relief amplitude. Coronae of class W rarely exhibit volcanic activity: the rift coronae – 5 of 20 (~ 25%) coronae and the pre-rift coronae – 17 of 139 (~ 12%).

Simple U-class depressions. The pre-rift coronae: 148 coronae total, about 16 of them exhibit volcanic activity, their average diameter is ~ 168±50 km, the average amplitude of vertical relief is ~ 0.7±0.2 km (table 1). The rift coronae: 17 coronae total, of them 5 are volcanically active. The average diameter of these coronae is ~ 287±80 km, the average amplitude of vertical relief is ~ 1.5±0.4 km. Coronae of the U class with annulus of different morphological types are significantly different in both the average diameter and the amplitude of relief. Coronae of the U-class rarely exhibit volcanic activity: the rift coronae – 5 of 17 (~ 29%) coronae and the pre-rift coronae – 16 of 148 (~ 11%).

Conclusions. Most of the coronae of Venus (~ 83%) are topographically mature pre-rift structures and only small fractions of them (~ 17%) are topographically immature features that are characterized by dome-shaped rises. (2) The older, pre-rift, coronae are less volcanically active compared to the young, rift-related, coronae. (3) For the all topographic classes, the amplitude of relief of the rift-related coronae are about two times larger of the amplitude of relief of the pre-rift coronae but the average diameters of the pre-rift and rift coronae are about the same. All these differences in the coronae morphometry may be reflect changes of the structure of lithosphere as a function of time. It is likely that the pre-rift coronae formed in the environment of a thinner lithosphere, whereas the rift-related coronae developed in the thicker-lithosphere conditions.

The study was carried out within the state assignment of the Vernadsky Institute of Geochemistry and Analytical Chemistry of the Russian Academy of Sciences (GEOKHI RAS).

References

1 Barsukov V.L., Bazilevsky A.T., Kuzmin R.O. et al. Geology of Venus based on the results of radar images obtained by AMS "Venus-15" and "Venus-16" (preliminary data). Geochemistry. 1984. (12). 1811-1820. (In Russ.).

2 Guseva E. N., Ivanov M.A. Coronae of Venus: geological, topographic and morphometric characteristics. Sol. Syst. Res. 2022. V. 56 (2). 76-83.

3 Guseva E. N., Ivanov M.A. Coronae-sources of young volcanism on Venus: topographic features and estimates of productivity. Sol. Syst. Res. 2024. V. 58 (1). 78-87.

4 Guseva E. N., Ivanov M.A. Spatiotemporal relationships of the groove belts, coronal structures, and rift zones of Venus // Sol. Syst. Res. 2019. V. 53 (6). p. 411-422.

5 Guseva E.N., Ivanov M.A. Spatial and genetic relationships of coronae, lobate plains and rift zones of Venus. Sol. Syst. Res. 2023. V. 57 (2). 112-121.

6 Barsukov V.L., Basilevsky A.T., Burba G.A., Bobinna N.N., Kryuchkov V.P., Kuzmin R.O., Nikolaeva O.V., Pronin A.A., Ronca L.B., Chernaya I.M., and 20 co-authors. The geology and geomorphology of the Venus surface as revealed by radar images obtained by Venera 15 and 16. JGR. 1986. V.91. B4. D378-D398.

7 Basilevsky A.T., Head J.W. Global stratigraphy of Venus: Analysis of a random sample of thirty-six test areas. EMP. 1995. V.66. 285-336.

8 Basilevsky A.T., Head J.W. Geologic units on Venus: Evidence for their global correlation. PSS. 2000. V.48. 75-111.

9 Crumpler L.S., Aubele J. Volcanism on Venus, in Encyclopedia of Volcanoes, Houghton B., Rymer H., Stix J., McNutt S., Sigurdson H. Eds. San Diego: Acad. Press. 2000. 727-770.

10 Ivanov M.A., Head J.W. Global geological map of Venus. PSS. 2011. V.59. 1559-1600.

11 Koch D.M., Manga M. Neutrally buoyant diapirs: A model for Venus coronae. GRL. 1996. V. 23. 3. 225-228.

12 Kreslavsky M.A., Vdovichenko R. Topography of Small Coronae on Venus: Preliminary Overview. Lar and Planet. Sci. XXVII. 1996. 699-700.

13 Nikishin A.M. Tectonics of Venus: A review. EMP. 1990. V.50/51. 101-125.

14 Pronin A.A., Stofan E. Coronae on Venus: Morphology and distribution. ICR.1990. V.87. 452-474.

15 Smrekar S.E., Stofan E.R. Corona formation and heat loss on Venus by coupled upwelling and delamination. SCI. 1997. V.277. 1289-1294.

16 Stofan E.R., Hamilton V.E., Janes D.M., Smrekar S.E. Coronae on Venus: morphology and origin. Venus II Geology, Geophysics, Atmosphere, and Solar Wind Environment. Eds: Bougher S.W., Hunten D.M., Phillips R.J. Tucson: Univ. Arizona Press, 1997. 931-965.

17 Stofan E.R., Sharpton V.L., Schubert G., Baer G., Bindschadler D.L., Janes D.M., Squyres S.W. Global distribution and characteristics of coronae and related features on Venus: Implications for origin and relation to mantle processes. JGR. 1992. V.97. E8. 13.347-13.378.

Krasilnikov A.S., Ivanov M.A. Determination of the mixing factor of local and foreign material in the langrenus, cavalerius and theophilus crater ejecta. *UDC 523.34*

Vernadsky Institute of Geochemistry and analytical Chemistry RAS, 119991, Moscow, Russia
krasilnikov_as@geokhi.ru

Abstract. Based on the data on the iron oxide and olivine content in the rays of the Langrenus, Cavalerius and Throphilus craters, a relationship has been definite that describes the ratio of the mare regolith to the material of the crater ejecta. This ratio represents a mixing factor of local and foreign material formed during the fall of craters ejecta. The data obtained make it possible to refine the currently existing mixing models.

***Keywords**: The Moon, Langrenus, Cavalerius, Theophilus, rays, ejecta, mixing factor*

Introduction: Determining the material mixing factor when impact crater ejecta are formed, is one of the main tasks, the solution of which will help to clarify our knowledge of the distribution of material on the Moon. Understanding of this distribution provides information on the composition and origin of certain ejecta. However, the existing models of ejecta emplacement and their mixing differ greatly, and therefore the material mixing factor needs to be studied further.

Mixing factor of local and foreign materials: There are a series of models (McGetchin et al., 1973; Pike, 1974; Fassett et al., 2011; Housen et al., 1983; Sharpton, 2014) that give a representation of the thickness of ejecta deposits, however, do not take into account the inevitable mixing of ejecta material with the underlying regolith. During the emplacement of ejecta deposit materials in a broad range of sizes fall out forming secondary impact craters of different diameters. As the result, the regolith of the near-surface layers is mixed with the ejecta material. The solution of the mixing problem was proposed in work by Oberbeck et al. (1975), where they presented the results of studies of quantitative evaluation of volume ratio of the local regolith to material of ejecta; they called it the mixing factor μ). Oberbeck et al. (1975) conducted a series of experiments and studied secondary craters on the Moon and they deduced an empirical relation of the change of μ as the function of distance from the crater:

$$\mu = 0.0183 \cdot R^{0,87} \qquad (1),$$

where R – distance from the middle of the crater radius to the point where μ is estimated.

Oberbeck et al. (1975) suggested that this relationship can be applied not only to determine the degree of mixing of ejecta from the Copernicus crater, but also for other large lunar craters. The R value was chosen to be equal to the distance from the middle of the crater radius to the calculation site because it is not possible to determine from which part of the crater a fragment, which caused formation of a secondary crater, was ejected.

In their work, Petro and Pieters (2006) compared the results of various ejecta deposition models, including models with and without material mixing. The authors determined that the results obtained using the mixing model of Oberbeck et al. (1975) are poorly comparable with the geochemical and petrographic features of the Apollo 16 soil (Korotev, 1997). This discrepancy led Petro and Pieters (2006) to the conclusion that the mixing factor μ calculated from formula (1) should be reduced by about a factor of two.

Estimation of the mixing factor by the data on FeO and olivine content in the rays of craters Langrenus, Cavalerius, and Theophilus

By the measurement settings, the model by Oberbeck et al (1975) is applicable to the larger fraction of ejected materials that is able to form secondary craters. How the mixing is changed for the ejecta fine-grain materials that form rays? In order to address this problem, we estimated the distribution of iron oxide and olivine from the data of the Clementine mission in the rays of craters Langrenus, Cavalerius and Theophilus (Fig. 1).

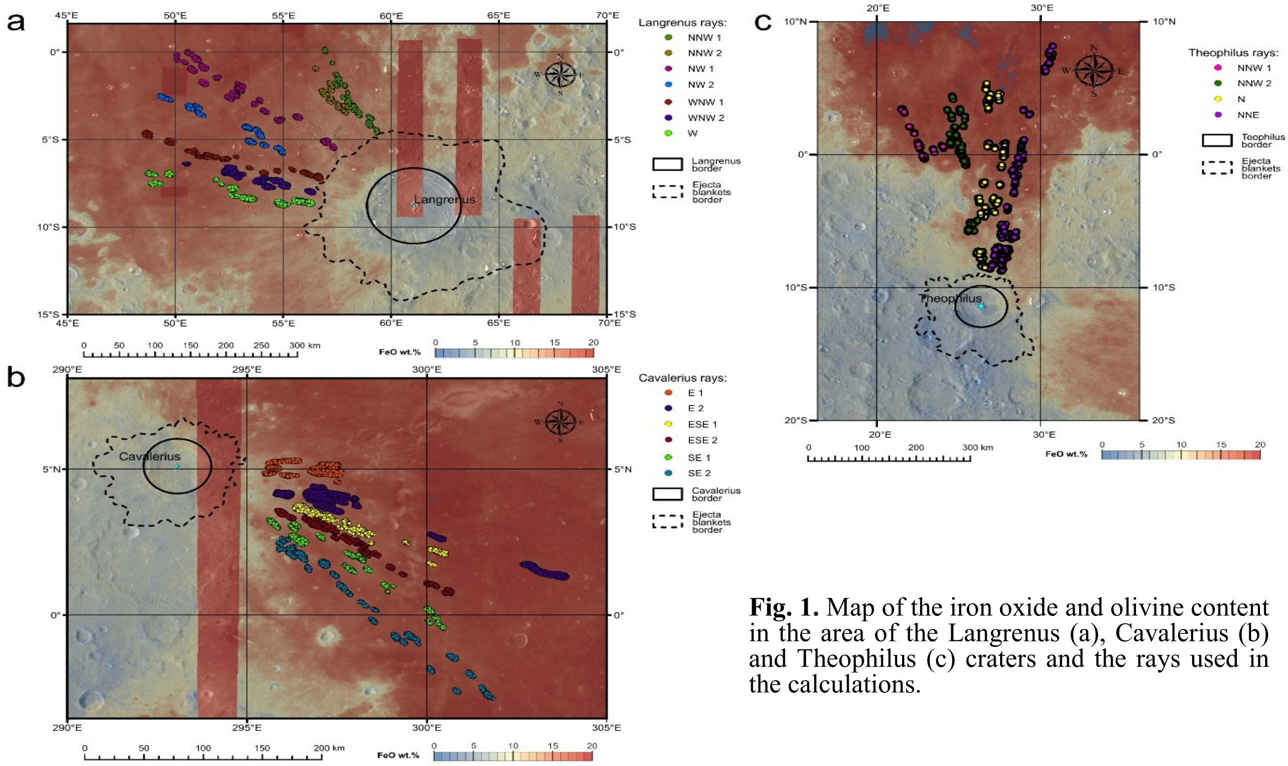

Fig. 1. Map of the iron oxide and olivine content in the area of the Langrenus (a), Cavalerius (b) and Theophilus (c) craters and the rays used in the calculations.

These craters have been selected because of the following reasons:

(1) they are located at the border of the mare and the highlands, and part of their rays are clearly visible on the dark and smooth mare surface;

(2) the ages of the Langrenus and Cavalerius craters are close to the ages of the neighboring maria, which minimizes the factor of the ray appearance by the mechanical disturbance of the regolith and emphasize the compositional difference between materials in the rays and the surrounding mare regolith. The age of the Langrenus crater, 3.44 Ga almost coincides with the age of the surface of Mare Fecunditatis in the region where the rays are visible, 3.37 Ga (Ivanov et al., 2023). The age of the Cavalieri crater is ~3.2 Ga (Hood., 1981), and the age of the Oceanus Procellarum nearby is 3.18 Ga (Stöffler and Ryder, 2001). We investigated the rays of crater Theophilus to test the influence of the mechanical factor in the rays formation.

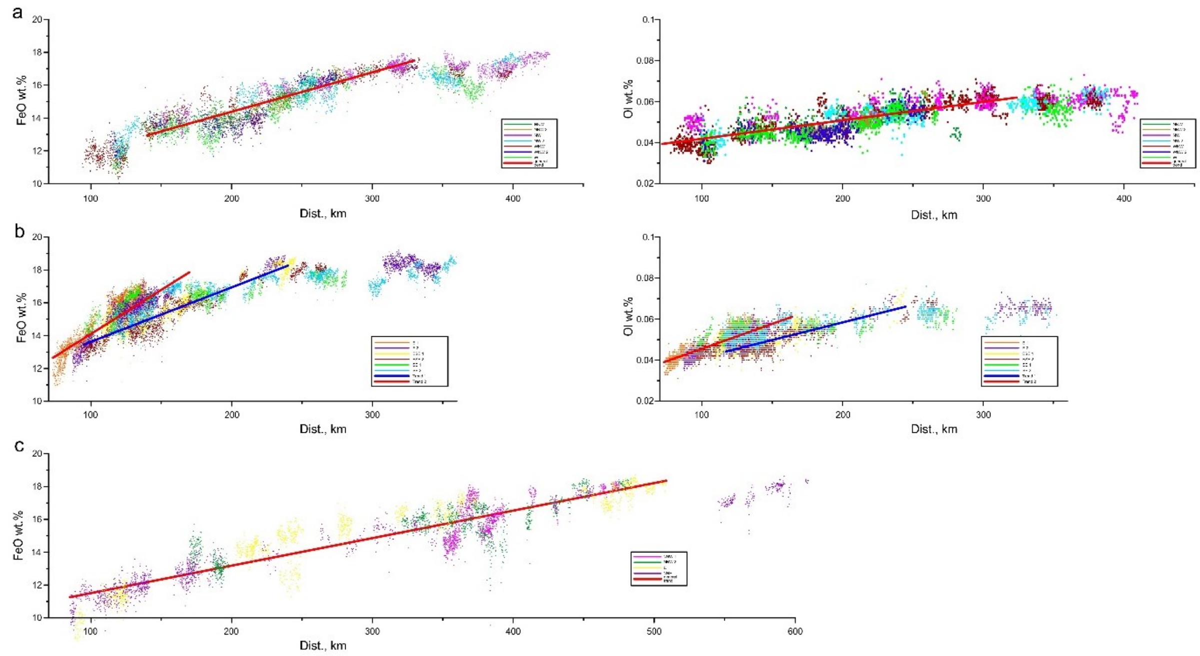

Fig. 2. Change in the amount of iron oxide and olivine in the rays of the Langrenus (A), Cavalerius (B) and Theophilus (C) craters depending on the distance from its center.

In our study, were used only those rays that lie on the smooth surface of the mare. Within each of them, were have selected randomly distributed points, at which the model iron oxide and olivine content was determined. The obtained data form a clear trends of increasing of the local (mare) material defined by its intrinsic components such as FeO and olivine as the distance from the center of the crater increases (Fig. 2). These trends are approximated by the following linear functions:

$$FeO = 2.47 \times 10^{-5} R + 9.33, \quad (2)$$

$$Ol = 8.99 \times 10^{-8} R + 0.03, \quad (3)$$

where R – distance from the crater center in meters.

At the distance of about three diameters of the Langrenus crater (~300 km), both trends are flattening and no increase in iron oxide and olivine content in the rays is observed. We consider the increase in iron oxide as a result of the mixing of two end members: mare material with an average FeO content of 17.5 wt.%, and highland materials with an average FeO content of 5.5 wt.%. The determined function (2) shows that immediately after the zone of continuous ejecta at a distance of ~150 km from the center of the crater, the content of iron oxide is ~13.16 wt.%, which, at the adopted contents of iron oxide in the end-members, corresponds to a mix of ~ 36 and 64% of the highland and mare components, respectively. At a distance of 330 km, where the horizontal part of the trend begins, the iron oxide content is estimated to be ~17.5 wt.%, which practically coincides with the average FeO content in the Mare Fecunditatis regolith and, therefore, corresponds to almost 100% of the mare component.

The obtained dependence (2) allows us to propose a formula for estimating the proportion of foreign/local material (L/F) in the range of distances from the zone of contiguous ejecta (~100 km) to the zone where the rays fade out (~300 km):

$$\frac{L}{F} = (2.1 \times D^{0,49})10^{-3} \quad (4)$$

where D – distance from the crater center in kilometers.

The olivine content of the rays of the Langrenus crater was considered in a similar way and the following formula was obtained:

$$\frac{L}{F} = (7.2 \times D^{0.8})10^{-5} \quad (5)$$

Iron oxide and olivine contents were also determined for rays from the Cavalerius crater. Their contents form two trends, the first of which is confined to the east-southeast rays and the second is related to the southeast rays. Presumably, the formation of these two trends is related to an oblique impact, which caused an asymmetric distribution of ejecta from the crater. A second hypothesis links their formation to the presence of magnetic anomalies in this part of the Oceanus Procellarum, leading to surface renewal. The resulting relationships can be described by the following formulas:

$$FeO = 3.31 \times 10^{-5} R + 10.32, \text{(trend 1)} \quad (6)$$
$$FeO = 5.59 \times 10^{-5} R + 8.43, \text{(trend 2)} \quad (7)$$
$$Ol = 1.71 \times 10^{-7} R + 0.03, \text{(trend 1)} \quad (8)$$
$$Ol = 2.43 \times 10^{-7} R + 0.02, \text{(trend 2)} \quad (9)$$

As in the case of the Langrenus crater, formulas were obtained for determining of the mixing ratio in the rays of the Cavalerius crater:

$$\frac{L}{F} = (3.9 \times D^{0.6})10^{-4}; (FeO, \text{trend 1}) \quad (10)$$
$$\frac{L}{F} = (4.3 \times D)10^{-5}; (Ol, \text{trend 1}) \quad (11)$$
$$\frac{L}{F} = (4.2 \times D^{0.8})10^{-5}; (FeO, \text{trend 2}) \quad (12)$$
$$\frac{L}{F} = (6.4 \times D)10^{-6}; (Ol, \text{trend 2}) \quad (13)$$

For the rays of Theophilus crater, only the iron oxide content was determined and only in rays on the surface of Mare Tranquillitatis because the surface of Mare Nectaris contains a large amount of ejecta from other craters. This resulted in the following dependence of the iron oxide content in the crater rays on distance:

$$FeO = 1.68 \times 10^{-5} R + 9.83, \quad (14)$$

The obtained formulas (4-5, 10-14) describe the tranportation and mixing of the ray-forming, fine-grained fraction of the crater ejecta that compose a significant portion of the crater redistributed material and represent foreign materials in the samples of lunar regolith. Being compared with the formulas derived by Oberbeck et al. (1975) and Petro and Pieters (2006) (Fig. 3), it can be seen that most of the obtained dependencies are closer to the values of the formula of Petro and Pieters (2006), rather than Oberbeck et al. (1975), although the estimates by Petro and Pieters are preliminary approximations. The values obtained from the analysis of the rays of the crater Theophilus stand out most strongly. Presumably, this is due to the large difference in age between the surface of the Mare Tranquilitatis (~3.4-3.8 (Hiesinger et al., 2000)) and the crater (1.1-3.2 (Wilhelms, 1987)).

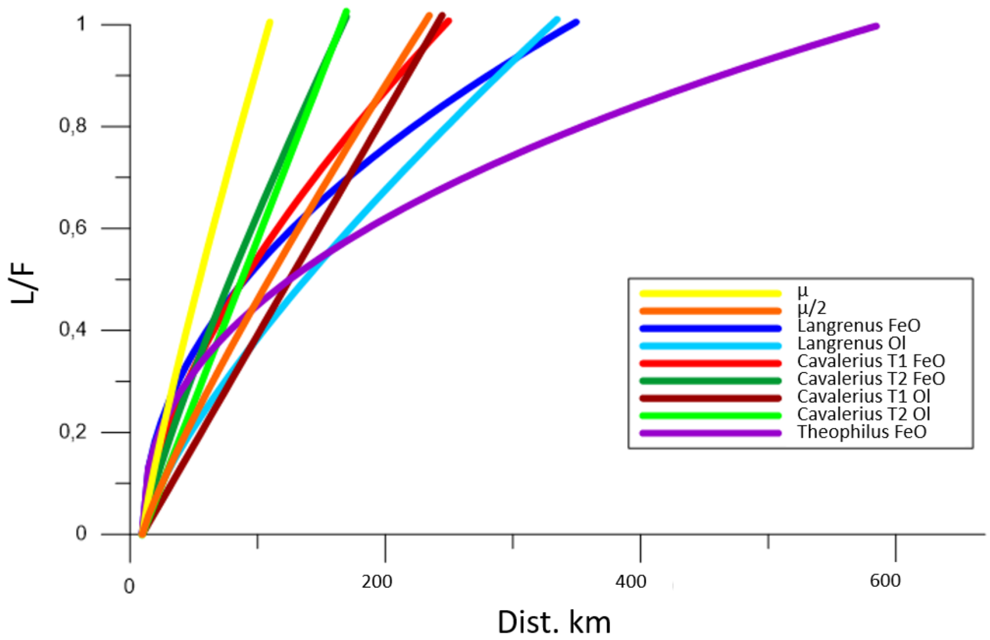

Fig. 3. Comparison of the obtained ratios of local and foreign material using the example of a crater with a diameter of 40 km.

Sources of funding: The work was done under the GEOKHI RAS state assignment.

References

Fassett C.I., Head J.W., Smith D.E., Zuber M.T., Neumann G.A. (2011) Thickness of proximal ejecta from the Orientale Basin from Lunar Orbiter Laser Altimeter (LOLA) data: Implications for multi-ring basin formation. Geophys. 38, L17201.

Hiesinger H., Jaumann R., Neukum G., Head J.W. (2000) Ages of Mare basalts on the lunar nearside. J. Geophys. Res. Planets 105, 29,239–29,275.

Hood L.L. (1981) The enigma of lunar magnetism. Eos, 62, 161–163. DOI: 10.1029/EO062i016p00161

Housen K.R., Schmidt R.M., Holsapple K.A. (1983) Crater ejecta scaling laws: fundamental forms based on dimensional analysis. J. Geophys. Res. Solid Earth 88, 2485–2499.

Ivanov M.A., Head J.W., Hisenger H. (2023) New insights into the regional and local geological context of the Luna 16 landing site. Icarus 400, 115579.

Korotev R.L. (1997) Some things we can infer about the Moon from the composition of the Apollo 16 regolith. Meteor. and Planet. Sci. 32(4), 447–478.

McGetchin T.R., Settle M., Head J.W. (1973) Radial thickness variation in impact crater ejecta: implications for lunar basin deposits. Earth and Planet. Sci. Lett. 209(2), 226–236.

Oberbeck V.R., Hörz F., Morrison R.H., Quaide W.L., Gault D.E. (1975) On the origin of the lunar smooth-plains. The Moon 12, 19–54.

Petro N.E., Pieters C.M. (2006) Modeling the provenance of the Apollo 16 regolith. J. Geophys. Res. 111, 1–13.

Pike R.J. (1974) Ejecta from large craters on the Moon: Comments on the geometric model of McGetchin et al. Earth and Planet. Sci. Lett. 23(3), 265–271.

Sharpton V.L. (2014) Outcrops on lunar crater rims: Implications for rim construction mechanisms, ejecta volumes and excavation depths. J. Geophys. Res. Planets 119, 154–168.

Stöffler D., Ryder G. (2001) Stratigraphy and isotope ages of lunar geologic units: chronological standard for the inner solar system. Space Sci. Rev. 96, 9–54. DOI: 10.1023/A:1011937020193

Wilhelms D.E. (1987) The geologic history of the Moon. USGS Numbered Ser. Prof. Pap. 1348, 302. https://doi.org/10.3133/PP1348.

Marakushev S.A. Geochemical roots and energy of metabolism. *UDC 553.21: 576.8: 577.37*

Federal Research Center for Problems of Chemical Physics and Medicinal Chemistry, RAS, Chernogolovka, Russia shukaram@yandex.ru

Abstract. The first forms of life in the hydrothermal conditions of the early Earth were apparently microorganisms with chemoautotrophic (chemolithotrophic) metabolism, using carbon dioxide (CO_2) as a carbon source and endogenous energy sources (H_2, H_2S). A biomimetic reconstruction of the early stages of evolution allows us to link the origin of four modern bacterial pathways for CO_2 fixation with a geochemical autocatalytic protometabolic network and trace their subsequent evolution. Thermodynamically, it has been shown that, under the influence of the chemical potential of molecular hydrogen, this network separates at bifurcation centers, forming phase spaces of stability for various types of autotrophic metabolism. The development of a proto-metabolic network in thermodynamically stable redox environments of hydrothermal systems led to the selective specialization of CO_2 fixation pathways, accompanied by the formation of original carbon dioxide binding mechanisms. These mechanisms became the metabolic basis for nascent bacterial communities and the driver of their consistent evolution, which was accompanied by a shift in metabolic energetics: from chemolithotrophy to anoxygenic photolithotrophy and, finally, to oxygenic photosynthesis—photoautotrophy, completely independent of endogenous hydrogen energy.

Keywords: *hydrothermal systems, metabolic reconstruction, bifurcation nodes, hydrocarbons, chemical potentials, CO_2 fixation pathways, chemotrophy, phototrophy*

Ancient hydrothermal systems served as geochemical reactors for the synthesis and transformation of metabolic network intermediates and were similar to modern mid-ocean ridge systems, with varying redox conditions (such as the predominance of H_2 or CO_2). The hydrothermal vent environment, rich in molecular hydrogen (H_2), hydrogen sulfide (H_2S), and hydrocarbons, is considered a likely site for the synthesis and self-organization of the first organic compounds into autocatalytic primary metabolic networks, which are the basis for nascent life. It is assumed that the original proto-metabolic network included four CO_2 fixation modules: three autocatalytic cycles—the 3-hydroxypropionate (**3-HP**) bicycle, the reductive pentose phosphate (**RPP**, or Calvin–Benson cycle), and the reductive citrate (**RC**, reductive tricarboxylic acid cycle, Arnon cycle)—and one linear pathway, namely the acetogenic acetyl-CoA pathway (**Acetyl-CoA**, Wood–Ljundgahl pathway). These modules encompass all known bacterial phylogenetic diversity and were a prerequisite for the emergence of chemolithotrophy, photolithotrophy, and photoautotrophy.

The presented reconstruction of the evolution of these systems is based on the modern concept that metabolic networks preserve relics of prebiotic chemical reactions of the abiotic carbon cycle—reactions that were catalyzed by organic molecules and minerals before the emergence of enzymes. Branching and diversification occurred in key intermediates of the protometabolic network, such as acetate, pyruvate, oxaloacetate, succinate, fumarate, and others, under the influence of external chemical potentials. These points of interweaving (bifurcation nodes) of metabolic network modules determined the entire compositional diversity of the emerging metabolism, and the chemical potentials of the environment created by ascending deep fluids in ancient hydrothermal systems could isolate specific carbon fixation systems within protometabolic networks and control their long-term evolution (Marakushev and Belonogova, 2013, 2019).

According to thermodynamic calculations (Marakushev and Belonogova, 2013; Kua et al., 2021) and biochemical studies of the metabolism of modern autotrophs (Berg et al., 2022), the bifurcation nodes were the following reversible equilibria: acetate ↔ pyruvate (1,5 $C_2H_4O_2 \rightleftharpoons C_3H_4O_3 + H_2$) – distributes electron flows between the acetyl-CoA pathway and the RPP cycle; and succinate ↔ fumarate ($C_4H_6O_4 \rightleftharpoons C_4H_4O_4 + H_2$) – distributes electron flows between the RC cycle and the 3-HP bicycle. Equilibria between these intermediates of the proto-metabolic network were regulated exclusively by the chemical potential of hydrogen. Previous studies have shown that reactions that form intermediates of the metabolic network and carry out their development are favored by the conditions of thermodynamic stability of specific hydrocarbons (Marakushev, 2008; Marakushev, Belonogova, 2021, 2026).

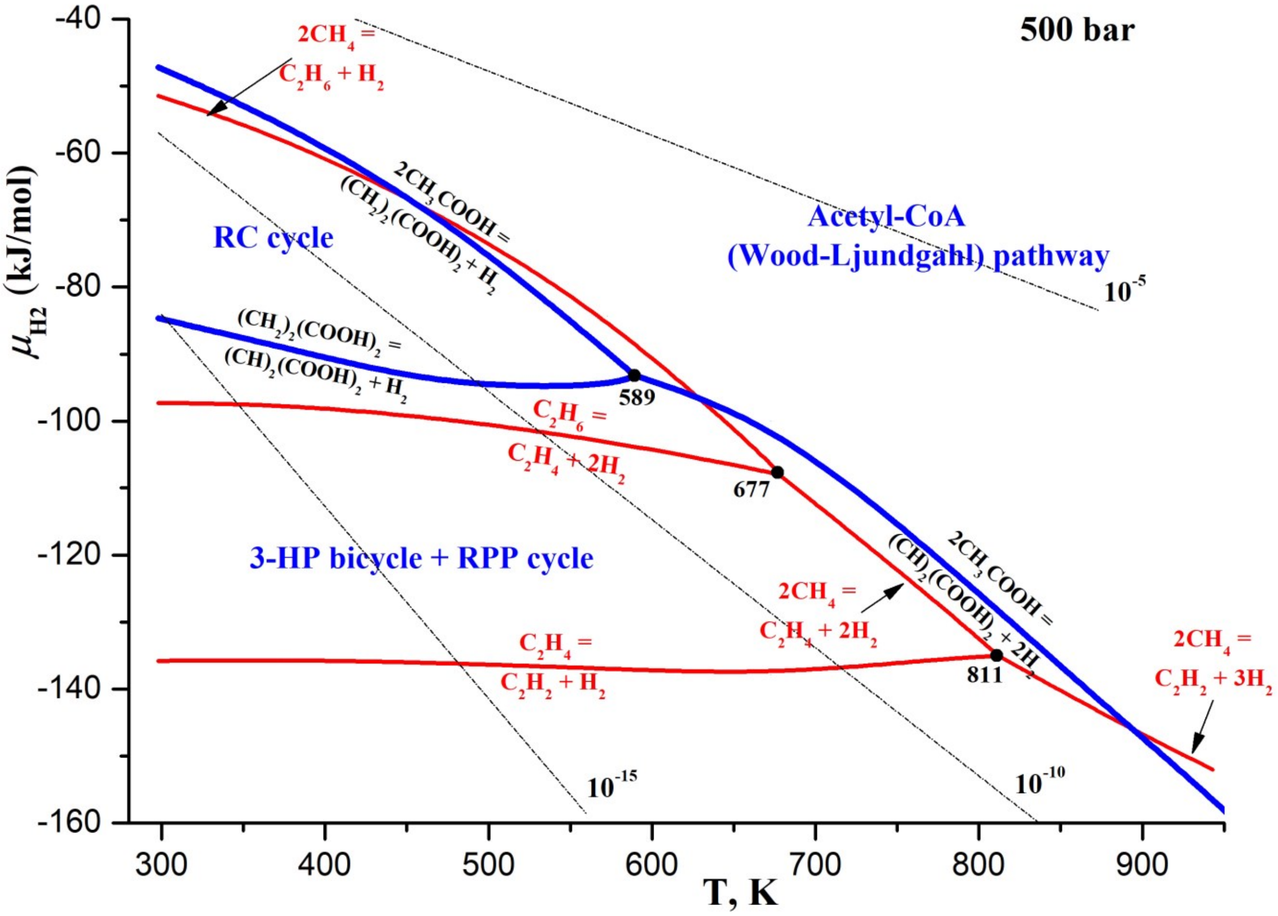

Fig. 1. Thermodynamic stability regions (facies) of aqueous hydrocarbons (ethyne, ethene, ethane, methane) and intermediates of bacterial CO_2 fixation pathways (aqueous fumarate, succinate, acetate) in a hydrothermal system on the diagram of the chemical potential of aqueous hydrogen (μ_{H2}) - temperature (T, K) at a pressure of 500 bar. The values of the free energy of formation of aqueous hydrocarbons are from (Oelkers et.al., 1995), and those of aqueous carboxylic acids are from (Amend, Shock, 2001; Marakushev, Belonogova, 2013 (Suppl. Mat)). The diagram was calculated using the Gibbs phase rule (Marakushev, 2008; Marakushev, Belonogova, 2009). The standard states used in the calculations were the unit activity of a hypothetical 1-molal solution, referred to infinite dilution at any temperature and pressure. The points on the diagram, marked by temperature, are three-phase invariant equilibria, coordinated by two-phase univariant equilibria (lines). The red lines delimit the stability regions of hydrocarbons, while the blue lines correspond to the facies of carboxylic acids—key intermediates in metabolic pathways.

The diagram chemical potential of hydrogen (μ_{H2}) - temperature (Fig. 1) shows a scheme of bifurcation and diversification of the protometabolic network. The diagram illustrates the combination of two aqueous thermodynamic systems: The C–H system (red lines) reflects the equilibria between alkynes (C_2H_2), alkenes (C_2H_4) and alkanes (C_2H_6, CH_4); The C–H–O system (blue lines) reflects the equilibria involving the key intermediates of bacterial CO_2 fixation pathways: acetate (CH_3COOH, acetyl-CoA pathway), succinate $(CH_2)_2$ $(COOH)_2$, reductive citrate (RC) cycle) and fumarate $(CH)_2$ $(COOH)_2$, 3-hydroxypropionate (3-HP) cycle). According to the works (Marakushev, Belonogova, 2016, 2026), fumarate, during its synthesis from non-methane hydrocarbons, forms a paragenesis with pyruvate ($CH_3COCOOH$), and therefore this phase space also determines the thermodynamic stability region of the reductive pentose phosphate (RPP) cycle. Monovariant equilibria of carboxylic acids (blue lines) separate divariant fields thermodynamically favorable for the synthesis and self-organization of the CO_2 fixation systems discussed below.

I. Acetyl-CoA pathway. The upper right high-potential corner of the diagram (Fig. 1) is occupied by the methane and acetate facies, which determines the phase space of thermodynamic stability of the high-potential acetogenic acetyl CoA pathway, which under these conditions can form both hydrogenotrophic ($2CO_2$ (aq)+$4H_2$ (aq) → CH_3COOH (aq)+$2H_2O$ (l)), ΔG^0_{298} = -169,38 kJ/mol) and methanotrophic (for example, CH_4 (aq)+$2HNO_3$ (aq) → 0·5CH_3COOH (aq)+H_2O (l) + $2HNO_2$ (aq), ΔG^0_{298} = -295,16 kJ/mol) metabolism (Marakushev, Belonogova, 2019). Metabolism, as the foundation for the emergence of life, shapes structural evolution at multiple scales—from the organization of the metabolic network to species-specific metabolic specialization and the molecular properties of enzymes (Moody et al., 2025). Consequently, the properties of enzymes catalyzing acetyl-CoA pathway reactions at early and subsequent stages of evolution must correspond to the reducing redox conditions under which precellular proto-metabolic CO_2 fixation systems functioned (Helmbrecht et al., 2025). The complete acetogenic acetyl-CoA pathway is found only in strict anaerobes and therefore possesses the most oxygen-sensitive enzyme of all CO_2-fixing enzymes: CO dehydrogenase/acetyl-CoA synthase (CODH/ACS). The acetyl-CoA pathway is the only CO_2 fixation pathway found in both bacteria and archaea, where the divergence of one-carbon metabolism led to the equilibrium transformation of methanotrophy into methanogenesis (Martin, 2020). The chemical antiquity of the acetyl-CoA pathway (Schoenmakers et al., 2024) is clearly reflected in its energetics. In hydrothermal systems, CO_2 reduction to form acetate is thermodynamically highly favorable; i.e., the acetogenic acetyl-CoA pathway is exergonic, allowing microorganisms with the most primitive redox physiology to generate proton-motive force for ATP synthesis through CO_2 reduction under ancient hydrothermal conditions (Martin, 2020).

II. Reductive citrate (RC) cycle. A significant progress in the evolution of the proto-metabolic network was its diversification with the selective isolation of the RC cycle, first proposed by Günther Wächtershäuser as the primary chemolithotrophic metabolic system (Wächtershäuser, 1990). In the network bifurcation diagram (Fig. 1), the RC cycle intermediates are thermodynamically stable in the aqueous ethane facies (upper left part of the diagram). An excellent biomimetic model of ancestral network metabolism, as part of a high-potential metabolite pool with respect to molecular hydrogen, is the metabolism of the hydrogenotrophic thermophilic bacterium *Aquifex aeolicus*, which fixes CO_2 via an incomplete form of the RC cycle linked to the acetyl-CoA pathway (Vázquez-Salazar and Muñoz-Velasco, 2025). This chemolithotrophic bacterium, which has one of the smallest genomes among known chemoautotrophs, can be considered a key candidate for reconstructing the anabolic metabolism model of LUCA (the last universal common ancestor), which was a hydrogenotrophic acetogen (Moody et al., 2024).

In the early stages of their development, living systems could obtain energy solely through the oxidation of geochemical molecular hydrogen and some other endogenous reducing agents (primarily H_2S). They were completely dependent on these sources, and therefore the spread of life was limited to the areas of strongly reduced hydrothermal vents. A crucial evolutionary innovation was the emergence of the ability of metabolic systems to obtain additional reducing energy directly from sunlight, eliminating their complete dependence on the hydrogen energy of the Earth's interior—namely, the emergence of photosynthesis. The most interesting biomimetic model of the metabolism of the first photosynthesising cell are the green sulfur chlorophototrophic bacteria *Chlorobi* (order Chlorobiales)—obligate anoxygenic anaerobic photolithotrophs that function in highly reducing conditions. These organisms are unique among photosynthetic phyla because they are the only ones to fix CO_2 via the branched reductive citrate cycle (RC) (Martin et al., 2018). Thus, the ethane facies (Fig. 1) is a thermodynamically favorable environment for the emergence and functioning of the photolithotrophic metabolism of green sulfur bacteria. The ancestral forms of these microorganisms, based on the hydrogenotrophic RC cycle, acquired reaction centers—the first light-dependent electron transport chains (Cardona, 2016). In other words, the first method of utilizing light energy in metabolism relied solely on the RC cycle as the primary metabolic foundation, ensuring the utilization of light energy, which became a significant factor in the evolution of the biosphere, Fig 2, left branch.

III. 3-hydroxypropionate (3-HP) bicycle. Diversification of the metabolite pool located along the bifurcation diagram in the low-potential (lower) region of phase space (Fig. 1) in a paragenesis with non-methane hydrocarbons (ethane, ethene, and ethyne) was accompanied by the formation of two hydrogenotrophic mechanisms of CO_2 fixation, based either on the 3-HP bicycle or on the reductive pentose phosphate (RPP) cycle (Marakushev, Belonogova, 2016, 2021).

The metabolism of green non-sulfur chemo- and photolithotrophic bacteria of the genus Chloroflexi, in particular the anoxygenic phototrophic *Chloroflexus aurantiacus*, can serve as a biomimetic model of a fragment of a metabolic network capable of self-organization into specific anabolic pathways (Nishihara et al., 2024). These pathways enable a shift from a chemolithotrophic to a photolithotrophic mode of nutrition (Kawai et al., 2022) under conditions characterized by a significantly more oxidative environment than that of the ancestral *Chlorobi*, whose metabolism relied on the reductive tricarboxylic acid cycle (RC cycle). However, this metabolism, based on the 3-HP and RPP cycles, remained dependent on endogenous geochemical hydrogen even after the acquisition of light energy, Fig 2, right branch. The emergence of the RPP cycle of autotrophic CO_2 fixation, possibly the very first means of incorporating phosphorus compounds into metabolism, revolutionized the evolutionary trajectory and metabolic energetics of nascent bacterial taxa. The enormous diversity of intermediates of the RPP cycle – pentoses and their utilization pathways, contrasting with the uniform structures of the hexose and citrate pathways – has significantly expanded the pool of intermediates and the number of reactions between them.

IV. Reductive pentose phosphate (RPP) cycle. On the early Earth, the expansion of ecological niches led to the separation of the low-potential part of the protometabolic network in the phase space of the 3-HP + RPP cycles (Fig. 1). Metabolic differentiation occurred between bacteria performing anoxygenic photosynthesis (*Firmicutes, Chloroflexi*) and cyanobacteria, the only prokaryotes that developed oxygenic photosynthesis involving the oxygen-tolerant RPP cycle for CO_2 fixation (Fischer et al., 2016; Martin et al., 2018; Nishihara et al., 2024). In the nascent taxon of photoautotrophic *Cyanobacteria*, the source of electrons and energy, instead of molecular endogenous hydrogen, became hydrogen obtained from water split in the reaction center of photosystem II (Fischer et al., 2016). Losing to hydrogenotrophic organisms in the competition for molecular hydrogen (Fig. 1) in their natural habitat, the ancestors of *Cyanobacteria* were forced to find another energy source. Replacing the endogenous energy source—hydrogen from the Earth's liquid core (Marakushev and Marakushev, 2010)—with an exogenous one (sunlight) allowed autotrophic metabolism to free itself from the direct dependence of its energy and evolution on hydrogen degassing from the Earth's interior. Thanks to this bioenergetic evolution, the RPP cycle has become the predominant mechanism by which cyanobacteria and all plants fix CO_2 using the key oxygen-resistant enzyme of this cycle, ribulose-1,5-bisphosphate carboxylase/oxygenase (RuBisCO). The RPP cycle is the most energy-intensive and inefficient of all bacterial autotrophic pathways for CO_2 fixation (Martin et al., 2018; Fischer et al., 2024). However, it is precisely this that necessitated the evolutionary emergence of photosystem II reaction centers, leading to a radical transition to an oxidizing environment, i.e., a significant expansion of the redox conditions of the biosphere.

The results of this analysis are summarized in Figure 2, which shows a diagram of the diversification of the autocatalytic proto-metabolic network leading to CO_2 fixation pathways in modern bacterial taxa.

Funding sources: This work was supported by a state assignment from the Federal Research Center for Problems of Chemical Physics and Medicinal Chemistry of the Russian Academy of Sciences, registration number 124020200104-8 (FFSG-2024-0004).

Acknowledgments*: I would like to thank the organizing committee of the "Khitariada-2026" Seminar for the opportunity to present and publish this paper.*

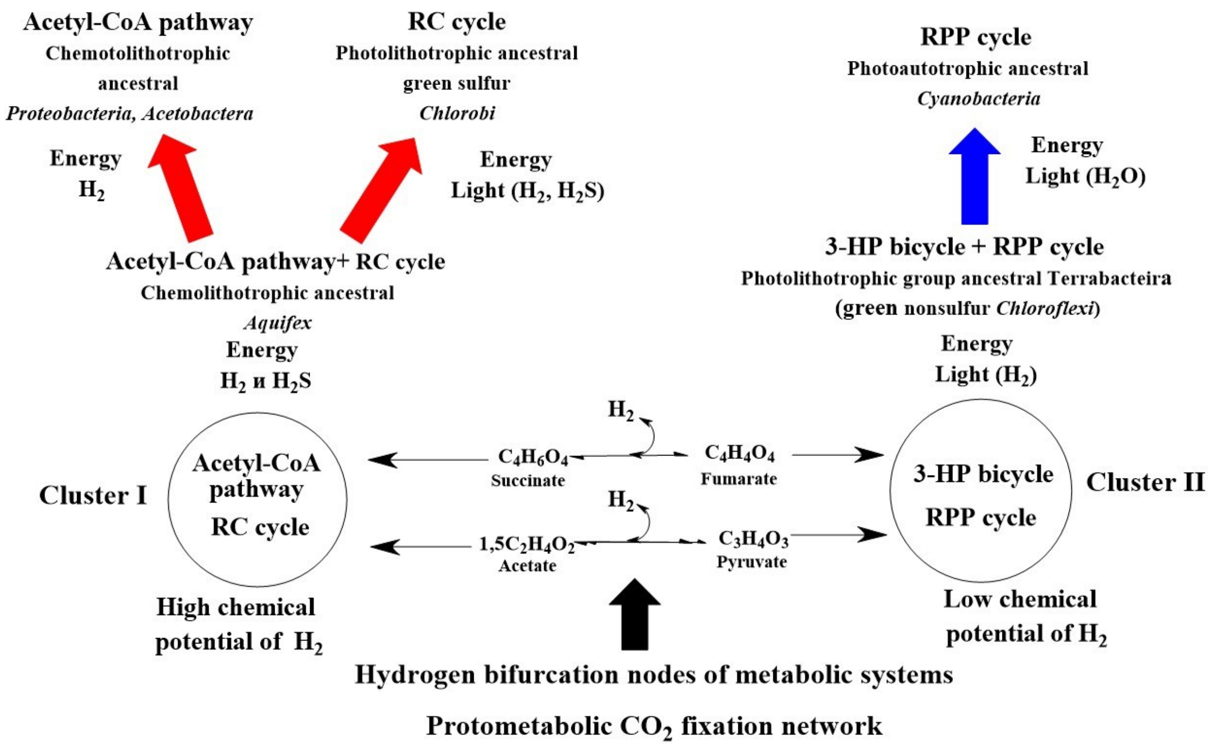

Fig. 2. Schematic representation of the diversification of the autocatalytic protometabolic network at key nodes of the electron flow bifurcation: succinate ⇌ fumarate and acetate ⇌ pyruvate. Red arrows indicate the evoluti on of the high-potential branch (RC cycle + Acetyl-CoA pathway) toward the ancestral taxa: *Proteobacteria, Acetobactera, Chlorobi, and Aquifex*. Blue arrows show the evolution of the low-potential branch (3-HP bicycle + RPP cycle) toward the ancestral *Chloroflexi* and *Cyanobacteria*. The carbon and energy substrates of the corresponding metabolic pathways are indicated to the left and right of the taxon evolution arrows.

References

Amend J.P., Shock E.L. (2001) Energetics of overall metabolic reactions of thermophilic and hyperthermophilic Archaea and Bacteria. FEMS Microbiol. Rev. V. 25. P. 175–243. https://doi.org/10.1016/S0168-6445(00)00062-0

Berg I., Mall A., Steffens L. et al. (2022) H_2 partial pressure switches autotrophic pathways in an anaerobic bacterium. https://doi.org/10.21203/rs.3.rs-1456100/v1

Fischer W.W., Hemp J., Johnson J.E. (2016) Evolution of Oxygenic Photosynthesis. Annu. Rev. Earth Planet. Sci. V. 44. P. 647–83. https://doi.org/10.1146/annurev-earth-060313-054810

Cardona T. (2016) Origin of Bacteriochlorophyll a and the Early Diversification of Photosynthesis. PLoS ONE. V. 11(3). e0151250. https://doi.org/10.1371/journal.pone.0151250

Helmbrecht V., Reichelt R., Grohmann D. et al. (2025) Simulated early Earth geochemistry fuels a hydrogen-dependent primordial metabolism. Nat. Ecol. Evol. V. 9. P. 69–778. https://doi.org/10.1038/s41559-025-02676-w

Kawai S., Shimamura S., Shimane Y. et al. (2022) Proteomic Time-Course Analysis of the Filamentous Anoxygenic Phototrophic Bacterium Chloroflexus aurantiacus, during the Transition from Respiration to Phototrophy. Microorganisms. V. 10. 1288. https://doi.org/10.3390/microorganisms10071288

Kua J., Hernandez A.L., Velasquez D.N. (2021) Thermodynamics of Potential CHO Metabolites in a Reducing Environment. Life. V. 11(10). 1025. https://doi.org/10.3390/life11101025

Lu X., Guoxia L., Fuyu G., Huawei Z. et al. (2022) Minimized Synthetic Carbon Fixation Cycle. ACS Catalysis. V. 12(1). P. 799–808. https://doi.org/10.1021/acscatal.1c04151

Marakushev A.A., Marakushev S.A. (2010) Fluid evolution of the Earth and origin of the biosphere. In: Florinsky, I.V. (Ed.), Man and the Geosphere. Nova Science Publishers Inc., New York, U.S.A. pp. 3–31. https://doi.org/10.13140/2.1.4787.9363

Marakushev S.A. (2008) Transformation of Hydrocarbons into Components of Archaic Chemoautotrophic CO_2 Fixation Cycle. Dok. Biochem. Biophys. V. 41P 18–23. https://doi.org/10.1134/S1607672908010055

Marakushev S. A., Belonogova O. V. (2009) The parageneses thermodynamic analysis of chemoautotrophic CO_2 fixation archaic cycle components, their stability and selforganization in hydrothermal systems. J. Theor. Biol. V. 257(4). P. 588–597. https://doi.org/10.1016/j.jtbi.2008.11.032

Marakushev S.A., Belonogova O.V. (2013) The divergence and natural selection of autocatalytic primordial metabolic systems. Orig. Life Evol. Biosph. V. 43. P. 263–281. https://doi.org/10.1007/s11084-013-9340-7

Marakushev S.A., Belonogova O.V. (2016) The Emergence of Bioenergetics: The Formation of a Gluconeogenesis System and Reductive Pentose Phosphate Pathway of CO_2 Fixation in Ancient

Hydrothermal Systems. Bioenergetics. V. 5(2). P. 233–238. https://doi.org/10.4172/2167-7662.1000141
Marakushev S.A., Belonogova O.V. (2019) Ideas and perspectives: Development of nascent autotrophic carbon fixation systems in various redox conditions of the fluid degassing on early Earth. Biogeosciences. V. 16. P. 817–1828. https://doi.org/10.5194/bg-16-1817-2019
Marakushev S. A., Belonogova O. V. (2021) Chemical basis of autotrophic carbon fixation paleometabolis m. Izv. RAN, Ser. Biol. V. 5. P. 453–463. https://doi.org/10.31857/S1026347021050097
Marakushev S.A., Belonogova O.V. (2026) Hydrocarbon Basis of Emerging Chemoautotrophic Metabolism (Thermodynamic Justification), Geochemistry International. V. 64(6). P. 431–444. https://doi.org/10.1134/S0016702925601639
Martin W.F., Bryant D.A., Beatty J.T. (2018) A physiological perspective on the origin and evolution of photosynthesis. FEMS Microbiol. Rev. V. 42(2). P. 205–231. https://doi.org/10.1093/femsre/fux056
Martin W.F. (2020) Older than genes: the acetyl CoA pathway and origins. Front. Microbiol. V. 11. 817. https://doi.org/10.3389/fmicb.2020.00817
Moody E.R.R., Williams T.A., Álvarez-Carretero S. et al. (2025) The emergence of metabolisms through Earth history and implications for biospheric evolution. Phil. Trans. R. Soc. B. V. 380. 20240097. https://doi.org/10.1098/rstb.2024.0097
Nishihara A., Tsukatanib Y., Azaid C. et al. (2024) Illuminating the coevolution of photosynthesis and Bacteria. Proc. Natl. Acad. Sci. USA. V. 121(25). e2322120121. https://doi.org/10.1073/pnas.2322120121
Oelkers E.H., Helgeson H.C., Shock E.L. et al. (1995) Summary of the apparent standard partial molal Gibbs free energies of the formation of aqueous species, minerals, and gases at pressures 1–5000 bars and temperatures 25–1000 °C. J. Phys. Chem. Ref. Data. V. **24.** P. 1401–1560.
Schoenmakers L.L.J., Reydon T.A.C., Kirschning A. (2024) Evolution at the Origins of Life? Life. V. 14. 175. https://doi.org/10.3390/life14020175
Vázquez-Salazar A., Muñoz-Velasco I. (2025) Evolutionary Routes to Modern Metabolic Pathways. Macromol. V. 5(2). 23. https://doi.org/10.3390/macromol5020023
Wächtershäuser G. (1990) Evolution of the first metabolic cycles. PNAS USA. V. 87(1). 200. https://doi.org/10.1073/pnas.87.1.200
Williamson M.P. (2024) Autocatalytic Selection as a Driver for the Origin of Life. Life. V. 14. 590. https://doi.org/10.3390/life14050590

Maxe L.P. Indicative characteristic of the shapes and morphology of metallic particles of cosmic dust formed in the Earth's atmosphere. *UDC 524-1/-8*

ALC «STRIM», Mogilev, Belarus, laramaxe@yandex.by

Abstract. Most entering cosmic dust (CD) is formed in the Earth's atmosphere during the destruction of meteoroids. Using images of micro-particles of CD, satellite information, video recordings, scientific publications, and information about meteoroids, the author examines the shapes and morphology of metallic particles of CD, linking them to the destruction of the initial meteoroid matter. Adopting the provisions of modern theories of deformation, plasticity of continuous media and their continuity, the author carried out a textural analysis of images of metal particles of CD usually detecting in planchets collecting CD particles that do not contain technogenic dust. Having considered the conditions of formation of CD particles in high-speed processes, the author concludes that the shapes and morphology of metal particles of CD are characteristic, indicating critical deformations during the destruction of meteoroid matter in the Earth's atmosphere. The revealed feature of CD metal particles can be used to solve applied tasks, in this work is used to search for traces of Tunguska space body, a cause of explosions of iron meteorites. The author analyzes satellite maps of the Tunguska explosion area, where spots of abnormal chromaticity (mosses, lichens) have been identified, and the assumption about the influence of layers of Tunguska CD on biogeochemical processes and presence of color spots.

Keywords: *meteoroid; shape and morphology; particles; cosmic dust; color; chromaticity; mosses; lichens; image analysis; Tunguska cosmic body*

Introduction. Asteroids, that becoming meteoroids have their own cosmic history. Asteroids were subjected to space weathering also destructive impact collisions that changed their moment of rotation and caused friction of their internal parts and their bodies were heated and cooled. They were affected by gravitational fields in deep space but especially when asteroids approached the Earth.

Meteoroids enter the Earth's atmosphere at hyper- or supersonic speeds, experiencing increasing aerodynamic drag, their substance is eroded. Meteoroids are completely destroyed by the atmosphere (they are observing as meteors) or partially (falling become as meteorites), becoming cosmic dust (CD) terrestrial born that settle on the surface of the planet. The particles of CD differ in their composition from meteoroids (asteroids, respectively), but they remain information carriers even in the absence of fragments of their original bodies on earth. Micro- and nano-sized metallic particles of CD could be different in their elemental composition, but they have common shapes and morphology. Metallic particles of CD are found on our planet in all accumulation planchets: sedimentary deposits, rocks, craters, and ice. Their presence on terrestrial surfaces and in geological layers indicates the destruction of meteoroid matter in Earth's atmosphere and forms constant background level of the CD. The destruction of meteoroids near or on the earth's surface leaves fragments – meteorites, but and layers of CD particles above the background values also indicate on traces of meteoroid events.

The goal, the task. Taking into account the variety and volume of information about the composition, shapes and morphology of particles of CD, the author identified a priority group – metallic particles of CD for textural analysis of their images. The aim of the work is to identify the formation patterns that determine the shapes and morphology characteristic of metallic particles of CD, indicating their near–Earth "birth" from meteoroid matter. To achieve the purpose of the work, based on the studies of CD by optical and electron microscopy (SEM), having formed a database of SEM images of metallic particles of CD, in this work the author set the task of conducting a textural analysis of images of metallic particles of CD, coupling with analysis of processes or phenomena that already having studied and during which shapes and particles are formed, similar to metallic particles of CD.

The object of textural analysis. The elemental composition of metallic particles of CD included in the image database is known. In the concept of texture in this work, regardless of the specific metal or alloy, according to the totality of features, the author has included the shape and morphology of metal particles of CD. Using the generated database of images of metallic particles of CD, the author conducted a textural analysis of the images, which revealed common basic primitives: stripes and waves, ridges and troughs, waves of ridges, micro-pores, ribbons. Textures of metal particles of CD includes "wave" parts, the morphology of the shapes is dominated by waves, cycles and their sequences of varying intensity and frequency. The "wave" textures include discrete shapes: micro shavings, layers of flakes, layers of plates, stacks of flakes, particles with elongated micro-pores, nano- and microspheres. Separate basic primitives and textures of metallic particles of CD were used for comparison with the textures of particles that are formed in the processes of plastic deformation and destruction of substances and materials under extreme conditions and loads.

Meteoroids, micrometeorites, metals in Earth's atmosphere. Massive meteoroids penetrate the Earth's atmosphere and do not often fly to collide with the surface, a significant part of the substance to the Earth micrometeorites deliver. Both, large meteoroids and micrometeorites undergo aerodynamic erosion. Micrometeorites, most often, erode to a complete loss of matter with the release of elements and supply the upper layers of Earth’s atmosphere with metal atoms: sodium, iron, nickel and others. Nickel atoms evaporate faster than iron atoms, and the smaller the size of iron micrometeorites, the faster the process of metal release into the upper atmosphere, respectively, increase Ni-emission. The agglomeration of molten particles slows down this process, reducing the evaporation surface area, and the emission becomes weaker (Devid et. al., 2019). Glow – metal emission is observed at an altitude of 90 km in a layer about 10 km thick, when illuminated by the Sun, as well as during ablation of meteoroids in Earth’s atmosphere.

“Preparation” at turbulence. Any meteoroid entering the atmosphere experiences increasing resistance and heats up, it is surrounded by plasma and is accompanied by a head shock wave, which it creates itself, and stochastic oblique compaction surges. Changes in air density, atmospheric turbulence, shock waves, and compaction surges act on the meteoroid body as a complex, shock-like, dynamic load, causing compression, displacement of internal parts, crushing, and friction. Partially, the products of destruction are carried into the atmosphere through the rear vacuum zone – behind the moving body, reducing the mass of the meteoroid and speed, and creating recoils (aftershocks). After shaking of meteoroid substance and separating of their pieces (micrometeorites) in the upper atmosphere, meteoroids acquire additional internal stresses and damage, depending on their mass and composition, initial velocity and trajectory. Most meteoroids do not have a well-streamlined shape and smooth surface; the erosion of their matter is accompanied by mass decrease carried away by particles of their destruction, gases, ions and atoms.

Deformation of metals. The continuity hypothesis. The theory of plastic deformation describes the phenomenon of plastic flow of metals during deformation and indicates the multilevel nature of the manifestation: on a macroscopic scale and microscopic. The texture represents microscopic metallic particles of CD, reflecting their common characteristic features – traces of plastic deformation and viscoplastic fracture. The texture makes it possible to identify local plastic deformation as a sign and shows that the phenomenon of local adiabatic shear (LocAS) is manifested in metallic particles of CD. The LocAS mechanism is represented as a rapid local cycle consisting of a plastic deformation of the material, the transition of work to heat, and thermal softening of the material. The discrete, fast-flowing LocAS cycle, repeated in sequences of cycles, is reflected in morphology of metallic particles of CD as bands of plastic shear, shear pits and cones of raptures. The LocAS mechanism satisfactorily explains these characteristic features of the shapes and morphology of metallic particles of CD. In some metallic particles of CD, micro-pores and elongated cavities are observed in the fracture area, this is not a typical type of fracture for metals. A similar pattern of fracture is observed in plastic polymers, manifesting itself as LocAS as a result of high-speed stretching of the deformable substance, which reaches the dynamic strength of the material. In this case, crazes occur in plastic polymers, they are formed when the polymer is stretched not into a vacuum, but into a filled of substance medium.

According to the continuity hypothesis, a body is considered as a continuous substance and a rapture of discontinuation of substance is prohibited – not allowed, that is, the substance does not allow the formation of a vacuum inside itself. In this paper, the continuity hypothesis is accepted as a working hypothesis.

The "reactor" of active zone is a source of CD. The author has put forward an assumption (hypothesis) that the transformation of meteoroid matter into CD particles and giving the shapes and morphology, occurs under special extreme conditions in a "reactor" that is some active zone of the meteoroid. Maximal parameters and gradients of pressure and temperature should be implemented in this zone, products should be introduced and periodically unloaded and high speed of performance should be ensured. Taking into account the above conditions, speed of movement and substance "preparedness", the active zone of meteoroids this is a boundary layer that differs from the "cultural" boundary layer of supersonic aircrafts in localization, size, uncontrollability, variability and instability of extreme parameters. The formation of metallic particles of CD by the mechanism of plastic deformation and the manifestation of LocAS in the form of strips and particles in the form of "shavings", Fig. 1 **A**, was considered by the author earlier (Maxe, 2024). Critical conditions (high temperature and pressure) make possible the phase and structural transformations of iron and carbon, which determines the shape and morphology of layered like "stacked" iron particles. The "stacks" look like layers of smoothly rounded plates, Fig. 1 **B**. Thin leaves-plates of scaly CD particles are formed by dissociation of compounds (for example, silver sulfide), silver films are separated by layers of melt (sulfur), forming flakes, Fig. 1 **C** (Piacente et al., 1990). But, metal alloys, melting, displace more fusible and volatile (easily evaporating) metals from pores-tubules (when stretched) and flat plates-flakes (under pressure).

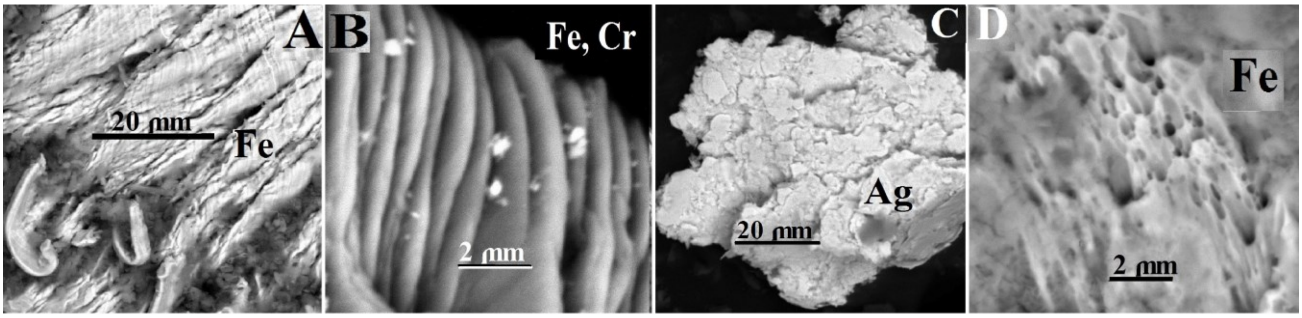

Fig. 1 A – iron "shavings"; B – "stacked" iron particles; C – flat scaly silver; D – "crazes" in a Fe-particle.

At supersonic speeds of meteoroids, the source of deformations and destruction in the active zone can be interaction of multiple turbulence streams, shock waves (SW) and appearing compaction surges with the boundary layer they both plasticize the substance flowing into boundary layer and deform it. The low-pressure region in backside (bottom) of bolide by SW and compaction surges stretches and tears the trapped layers of the substance, Fig. 1 **D**.

On micro-scale, the presence in metallic particles of CD elongated "crazes" that characteristic for deformable plastic polymers, the continuity hypothesis explains satisfactorily: vacuum inside the metal is prohibited, but is allowed forced filling of prohibited vacuum. On a macro scale, fracture pits and cones are characteristic for deformable plastic metals (Chegurov and Sorokina, 2018). In a macro-scale characteristic deformation picture of superplastic meteoritic iron is shown in the previously published paper (Maxe, 2025).

The formation of elongated micro-pores in the stretch-crashing meteoritic iron particle, Fig. 1 **D**, which initially was isolated from the external environment by an active zone, indicates that plastic deformation of the particle led to the formation of "crazes". Forbidding vacuum keep metal (or alloy) solid until a destruction moment of continuity by the way of release any available atoms into vacuum. In meteoritic iron, only nickel (or impurity) can be as filler for vacuum void. Nickel has the property of sublimating into a deep vacuum (that is used in metal refining), nickel "leaks" to the surface of asteroids heated by the Sun and sublimate, nickel sublimates from comets and their tails. Particles of meteoritic iron, deformed by stretching, self-filling the "crazes" with nickel atoms (to a certain value) and at destruction release hot nickel vapor into the atmosphere. Thus in the lower layers of the atmosphere, the erosion of meteoroid matter is accompanied by the emission of nickel atoms and by their glow in the visible range. An atmospheric "method" of visualizing the emission of nickel displaced from a falling meteorite fireball was observed in Japan, and it was recorded on video by automatic cameras (Meteor/Fireball, 2026).

Emission and visualization. Part of the luminosity of meteoroids is provided by evaporation of the meteoroid's substance, in this part metals, including nickel, iron, and sodium, can be identified in the optical range in emission spectra (by some way registration). The glow of the meteoroid in the visible range is cumulative and includes the radiation of all excited atoms. The predominance of a single color in the glow of a meteoroid or its trace, corresponding to the color of the lines of characteristic radiation of atoms of a certain element, indicates the predominance of atoms of this element in the radiation source. To observe the prevailing radiation, the emission of nickel atoms, very informative are the video recordings of the meteoroid flyby in Russia on October 27, 2025 and the meteorite impact on Mount Fuji in Japan on February 9, 2026.

Video footage of a meteorite falling on Mount Fuji, captured by an automatic camera located behind the mountain, provided unique information (Meteor/Fireball, 2026). The glow of atomic nickel (turquoise) prevails in the globular "cloud" behind the small bright "head" of the meteorite remnant approaching the mountain. A band of low clouds bent by a shock wave absorbs the turquoise "cloud" of the meteoroid. Accompanied by many fragments, the meteorite still hot but already "stripped", crashes into Mount Fuji without an explosion.

The decrease in the brightness of the glow in the central part, noticeable initially in the first two freeze frames, is probably due to the presence of radiation-absorbing particles in the turquoise globular "cloud". In the last two freeze frames, the globular "cloud" spread over the relief, the turquoise glow faded, therefore, the dust particles from the "cloud" covered all open surfaces, all active atoms reacted and stopped emitting. Vaporous nickel is active and could oxidize in lower atmosphere, once on a cold surface they could condense.

Fig. 2. Freeze-frames of the meteorite impact on Mount Fuji, Japan, February 9, 2026**.**

Traces of CD. Particles of CD, being products of the destruction of meteoroids in planet atmosphere, supply and enrich our Earth with matter. Particles of CD isolated from sedimentary rocks, sediments in water basins, deposits on ice and surfaces are significant source of information. When involved in the processes of biogeotransformation, particles of CD leave a multi-stage trail: they can "stain" the soil and water of rivers and water basins, affect the pigmentation of leaves of higher plants, mosses, and lichens. However, the particles of CD that consist of pure like "refined" metals that were settled as trace from the meteoroid these particles are able to persist for a long time, unchanged, in sedimentary layers and rocks deep underground.

Tunguska cosmic dust. The questions of what form substance remains, whether it can be found, and how the substance of the collapsed Tunguska cosmic body (CB) could "manifest" on Earth are not removed from discussion. It was decided to apply the applied aspect of the indicative characterizing of metallic particles of CD to search and analyze the manifestations of Tunguska cosmic substance – specifically, to settled CD.

In addition to the testimony of eyewitnesses who observed and felt the physical phenomena accompanying the Tunguska explosion on June 30, 1908, the data of the search operations and the results of the sample study, satellite maps and photographs of the explosion area are currently available. For the search and comparative analysis was used open information about recorded explosions smaller than the Tunguska CB one: Chulymsky CB on February 24, 1984 and Uchursky CB on August 3, 1993. Fragments of the destruction of the Chulymsky CB and Uchursky CB have not yet been found. No fragments of the Tunguska CB have been found also, but they could have formed during the explosion (of solid part). If they reached the surface, at present they remained at some depth, in a layer affected by the head shock wave and fires.

In craters and impact sites of large CB in addition to magnetite microspheres, researchers often find particles of solidified silicate and metal melts, and metallic particles of CD. If the core of the Tunguska CB was iron or ironstone, then its disintegration in Earth's atmosphere produced a huge amount and big mass of iron–containing particles and other CD, which settled in the wake along the trajectory irregularly in local spots, the location of which could shift for past time.

Assuming the presence of a special subsurface layer containing CD particles and, possibly, fragments, a special task was set – targeted monitoring of satellite maps of selected territories. It was decided to carry out a textural analysis of satellite images of the CB explosions areas (Tunguska's, Chulymsky, Uchursky), suggesting that color and/or chromaticity anomalies may be manifestations of the effect of the Tunguska CB substance on the phytobiocenosis. When solving the search problem, images and "Google.map" actual satellite maps were used. The dominant color and chromaticity of the images were associated with the chromaticity of the elements of the natural environment and objects in a certain particular place. Along the trajectory of the Tunguska CB, a depression was noted, highlighted by the Google option (Relief mode), which coincided with the conditional "butterfly" zone (the area of impact of the Tunguska CB explosion, which was determined by the evidence and results of the expeditions).

In the process of monitoring and analyzing satellite data, images of the Tunguska CB explosion area, local color spots (anomalies) were identified, distinguished by a structural organization, surrounded by a colored border, differing in color/chroma from the surrounding general background – phytocenosis and landscape, Fig. 3.

The explosion of the Tunguska CB occurred in a climatic zone where permafrost soils are not deep (from 50 cm). The area of the fall and the explosion site of the Chulymsky CB are located in a swampy area on the conventional line of retreat of permafrost soils. On satellite maps of the Chulym river area, at the confluence with the Ob, local color spots were found, similar to those identified in the area of the Tunguska CB explosion, but they are blurred and less localized. The fall and explosion of the Uchura CB were marked, the area is located outside the permafrost zone probably this factor explains the absence of abnormal in color spots: a different climatic zone, mountainous terrain. Targeted image monitoring allows suggest that permafrost soils in the Tunguska CB explosion zone is a most possible cause of anomalous colored spots.

Fig. 3. The explosion place of the Tunguska CB is marked with coordinates. Spots of color anomalies.

The search monitoring of images was carried out without reference to the color of a specific biological object. A comparative analysis of satellite images and photographs allowed find an appropriate "object". According to the range of natural pigmentation, mosses and lichens are closest to the abstract indicator used, taking into account biology (structure, nutrition, growth, reproduction) and unique features. Lichen is a symbiont of fungi and plants, it is highly adaptable, capable of accumulating heavy metals, and has its own "black body". Lichens grow slowly on rocky and rocky foundations and cold frozen soils, but they create a substrate that is necessary for mosses and other higher plants. Lichens are used as indicators of environmental pollution. Moss is able to absorb water, becomes almost white (yagel) when drying, and serves as an indicator of humidity. A change in pigmentation of lichens indicates adaptation to changed environmental conditions. In the taiga, locally altered environmental conditions are observed in areas of deforestation, windbreaks, hurricanes, pest damage, fires, and in any open area. After the usual fires, the taiga forest recovers slowly (about 100 years) the vacant place is first populated by lichens and mosses, later grasses, shrubs, trees. On free tops of the hills in the area of the Tunguska CB explosion, there are open areas, fallen forests, moss, but no color anomalies have been detected.

The development of the territory by slow–growing lichens and mosses in local spots may be due to the temperature of the underlying subsurface layers – frozen peat bogs. Excluding reasons man-made (cellars, glaciers) and technogenic thermal stabilization of soils (thermosiphons), the formation of anomaly spots can be explained by allowing of the formation of "shielding" layers in peat bogs containing settled matter of the Tunguska CB. An example: when a metal coating or metal particles are deposited or applied to the insulating surface, a surface is formed that shields radiation from the visible and thermal range. Similarly, in the case of deposition of CB matter and metal particles of CD onto peat compressed by a head shockwave, a multilayer "sandwich panel" with multiple reflections is formed. Among the metallic particles of CD, the best reflectors are scaly and lamellar particles with a mirror shine. A porous peat "sandwich panel", including metal particles of CD, having multidirectional cooling and heating flows, can effectively prevent the warming of frozen soil in a short summer and top soil cooling during a long low-temperature winter.

Conclusion. Metal particles of CD formed in the active zone of a meteoroid under extreme conditions, where the adiabatic shift localization – LocAC is manifested in the shape and morphology of these particles of CD, giving them a special indicative characteristic due to their origin.

Particles of CD that consist of pure iron, similar in shape and morphology to scaly, lamellar ones, tubular are indicative and characteristic because they are formed during the ablation of cosmic iron that is cosmic alloy of iron with nickel (kamacite/tenite). One reason of iron meteorites explosion in air (under tension load) and upon impact (at compression) could be release of atomic nickel, appear and accumulation of hot Ni-vapor.

CD participates in biogeochemical processes, which sometimes manifests itself in the environment and is recorded by satellite systems. The detection of particles in the settled cosmic dust layer of the Tunguska CB, similar in shape and morphology to the particles of ablation of cosmic iron, will indicate that the Tunguska CB had a containing iron core.

Not only as certain indicator the indicative characteristic of the shapes and morphology of metal particles CD may be used but it has informational volume and it can be used for solving problems in materials science, in the design and operation of devices, in additive technologies, in the development of protective materials, housings, shells, coatings.

References

David L. Bones, Juan Diego Carrillo-Sanchez, Alexander N. Kulak, John M.C. Ablation of Ni from micrometeoroids in the upper atmosphere: Experimental and computer simulations and implications for Fe ablation. Planetary and Space Science 179 (2019) 104725.

Maxe L. P. Shape and morphology of cosmic dust particles as manifestation of the adiabatic shift. // Experiment in Geosciences. 2024. Volume 30. N1. P. 17 – 21. https://www.iem.ac.ru/experiment/pdf/2024/p1.pdf

Maxe L. P. Morphological analysis of fragments: object, explosion, iron bolide hypothesis. // Experiment in Geosciences. 2025. Volume 31, N1. P 29 – 32. https://www.iem.ac.ru/experiment/pdf/2025/p1.pdf

Meteor / Fireball Lights Up Over Mount Fuji. 2026. [Электронный ресурс] URL: https://www.youtube.com/watch?v=QFp3Fzm3CMA&t=5s (дата обращения: 21.06.2026)

Chegurov M.K., Sorokina S.A. Fundamentals of fractographic fracture analysis of structural alloy samples: textbook. manual / M.K. Chegurov, S. A. Sorokina; NSTU named after R. E. Alekseev, Nizhny Novgorod. – 2018. – 79 P.

Piacente V., Scardala P., Ferro D. Study on the thermal decomposition of Ag_2S. Journal of materials science letters, 9 (1990), P 365 – 367.

Tselmovich V.A.,[1] Kamyshov A.N.[2] Detection of hydrogen in an archaeological artifact.

UDC 551.12; 549.2; *552.31;* 54-11; 54-18

[1] Borok Geophysical Observatory Institute of Physics of the Earth, Russian Academy of Sciences, Borok settlement, Yaroslavl region, Russia, tselm@mail.ru
[2] Baltic Escort Holding

Abstract. An archaeological artifact—a hammer composed of technically pure iron (TPI)—was discovered. Meteorites containing iron of such purity are unknown, and ancient metallurgists lacked the technology to produce TPI. Therefore, it became necessary to consider other possible origins. The study sought to demonstrate that the artifact was not made of smelted steel or a meteorite, but rather of a naturally occurring material. It was hypothesized that the hammer's metal may contain a large amount of hydrogen. Analysis confirmed this hypothesis: an abnormally high hydrogen content was detected in the sample. Tests were conducted using an AV-1 hydrogen analyzer. The mass fraction of hydrogen was determined using the vacuum heating method in accordance with GOST 21132.1-98. The results support the assertion that the find is of natural origin, associated with the formation of native metals in the Earth's crust through the interaction of hydrogen with basaltic melts. This finding supports V.N. Larin's hypothesis of a primordial hydride Earth. This discovery, with its analytical justification, is the first, but it cannot be isolated. The search for new objects is possible due to the fact that the discovery exhibits superplasticity, which may serve as a criterion for searching for new samples of hydrogenated iron.

Keywords: *commercially pure iron, hydrogen, metallurgy, natural native iron, meteoric iron*

Introduction. Surviving ancient literary sources claim that in ancient times, two types of iron (Fe), which could have been of cosmogenic or terrigenous origin, were used to create tools:

1. Cosmogenic iron. The Emir of Bukhara ordered his best armorers to forge him a sword from a piece of "heavenly iron." But no matter how hard they tried, nothing came of it. The heated iron was unforgivable, and the Emir executed the unsuccessful ones (Mezenin, 1985). This piece likely consisted of nickel-iron, which is difficult to forge.

2. Native iron. In his report of 1646, the Yakut voivode Vasily Pushkin wrote: "The Yakut foreigners, their Yakut iron, is the best, and they smelt that iron from stones, not in large quantities, not for great projects" (Nikolaev, 2021). In 1660, the Polish captive Kamensky-Dluzhik wrote that the Yakuts were collecting iron in piles along the banks of the Lena River, and that it was as good as steel. Ross's polar expedition in 1818 discovered that the Eskimos of Baffin Island were making knives and harpoon tips from iron they separated from a large meteorite lying on the shores of Melville Bay. A reference to this has been preserved in V. Levshin's "Commercial Dictionary" (Dictionary, 1787): "This is the name given to iron completely prepared by nature in the bowels of the earth and so completely purified of foreign substances that all manner of things can be forged from it without remelting. G. Ruel, through the East India Company, obtained a piece of such native iron from Senegal, where it is found in enormous blocks" (Mezenin, 1985). Native iron is found in many places in Siberia, a finding also noted by the authors of the article (Tselmovich et al., 2025).

It has been established (Tomshin et al., 2023) that "on the Siberian Platform, trap intrusions containing native iron are widespread. Iron occurrence is confined exclusively to intrusions whose magma fractionated in a deep (approximately 40 km from the paleosurface) intermediate chamber. In the intermediate chamber environment, the fluid-magmatic interaction of basaltic melt with high-temperature intratelluric fluid with reducing properties disperses the initially homogeneous basaltic fluid into silicate- and metallic-based liquates. It was the finely dispersed state of the fluid-magmatic system that determined the occurrence of native elements, primarily iron."

The possibility of the formation of native metals in the Earth's crust through the interaction of hydrogen with basaltic melts has been experimentally demonstrated (Persikov et al., 2019; Persikov et al., 2023). A new study (Huang et al., 2026) showed that the Earth's core may contain enormous hydrogen reserves, equivalent to a volume of 9 to 45 oceans.

The paper (Glazyev et al., 2023) "presents the results of experimental studies of hydrogen degassing from the Earth's interior—the cause of atmospheric ozone depletion, the content of which, in turn, determines the temperature and pressure of surface air. Spatial and temporal correlations between hydrogen degassing and ozone depletion, as well as the influence of the gravitational forces of the Moon and the Sun on degassing, provide the first opportunity for long-term forecasting of meteorological changes and the occurrence of climate disasters. The need for changes in climate and energy policies is substantiated." Given the enormous interest in both hydrogen degassing and TPI finds, an archaeological find—a 5-kg hammer (Fig. 1a) found at a depth of approximately 1 meter in the Sharya district of the Kostroma region (Morozovo site)—was studied. The hammer, composed of pure metallic iron (Fig. 1b), was discovered. The study was conducted using a Tescan Vega3 scanning electron microscope and an Oxford Instruments energy-dispersive spectrometer (EDS). The dominant phase in the X-ray diffraction spectrum of the iron studied is body-centered cubic iron (BCC iron).

Object and Methods of Study. Hydrogen mass fraction in a pure iron sample (hammer) was determined by vacuum heating in accordance with GOST 21132.1-98 at the Scientific and Production Complex Electronic and Beam Technologies (NPK EPT LLC) using an AV-1 hydrogen analyzer, certificate No. RU.C.31.001.A. When calibrating the analyzer, 4 standard samples of aluminum alloy composition of the AMg6 type (H2-PT-0.109), GSO 11164-2018, type approval certificate RU.C.01.494.A №. 5761, certified value of the mass fraction of hydrogen Qatt = 0.109 ± 0.015 [ppm] ± 13.8% with a confidence probability of P = 0.95 and 1201 (H2-PT-0.082), GSO 11163-2018, type approval certificate RU.C.01.494.A № 5760, certified value of the mass fraction of hydrogen Qatt = 0.082 ± 0.015 [ppm] ± 18.3% with a confidence probability of P = 0.95. Average sample weight was 2.05 g.

Test Procedure: To determine the mass fraction of dissolved hydrogen, three samples of different shapes were submitted (Fig. 1c). The initial sample, №. 1, was irregularly shaped. Two rectangular samples, №.2 and 3, were made from the second sample, a plate. The third sample, a forged plate, was №.4.

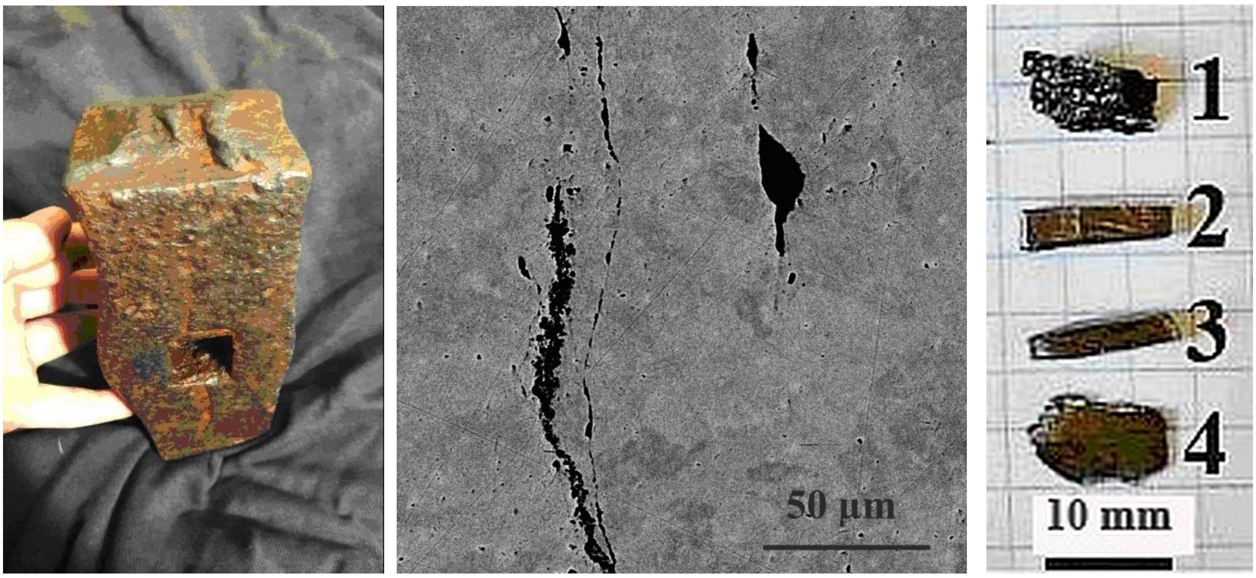

a) b) c)

Fig. 1. a) General view of the hammer; **b**) SEM image of a section of pure iron (BSE mode, high contrast); **c**) shape of the samples for analysis**.**

Experimental Procedure. The extraction system was prepared with careful removal of water. The analyzer was calibrated using state standard samples, GSO types AMg6 and 1201, at a temperature of 530°C. The hydrogen content in the samples was determined at extraction temperatures of 530°C and 800°C. The results of the experimental determination of the mass fraction of dissolved hydrogen in the samples are presented in Table 1. The letter Qp denotes the mass fraction of dissolved hydrogen at different extraction temperatures. The letter Q denotes the total dissolved hydrogen content.

Table 1. Test results**.**

Sample (Fig. 2)	Marking	Weight, g	Qp530 °C, ppm	Qp800 °C, ppm	Q, ppm
1	Original	0,522	4,720	1,383	6,103
2	Plate 1	0,549	0,549	0,258	0,807
3	Plate 2	0,518	0,452	0,270	0,722
4	Forged	0,167	3,381	0,837	4,218

Comments on the measurement results presented in Table 1.

1. Estimated uncertainty in the results of determining the total hydrogen mass fraction in samples № 1-4. The relative calibration uncertainty of the AV-1 hydrogen analyzer is determined by the uncertainty of the certified value of the AMg-6 alloy state standard sample and is ±13.8%. The systematic uncertainty of the analyzer is 6%, and the standard deviation of the random component of the device is ±3%. The expanded uncertainty with a coverage factor of k = 2 is ±6%. The total uncertainty determined by the contribution of these uncertainties is

$$\delta_{\sum} = \sqrt{13,82 + 52 + 62} = \pm 15,9\%$$

The results obtained for the 4 samples studied can be represented as:

$Q_1 = (6.10 \pm 0.97)$ ppm; $Q_2 = (0.81 \pm 0.13)$ ppm; $Q_3 = (0.72 \pm 0.12)$ ppm; $Q_4 = (4.22 \pm 0.67)$ ppm. Let us compare the results for samples № 2 and №. 3. The difference $Q_2 - Q_3 = (0.81 - 0.72)$ ppm = 0.09 ppm < ΔQ_2 and ΔQ_3, therefore, the results can be averaged: $Q_{23} = (0.76 \pm 0.18)$ ppm. The obtained result can be compared with the results of the Armco iron study: 0.13- 0.15 ppm – material as received, 0.30 ppm – in the destruction zone. The Q_{23} value is 5.4 times higher than the mass fraction value in Armco iron. Similar as-received hydrogen mass fraction values hydrogen (0.1 ppm) were obtained at NPK EPT for low-carbon S-20 pipe steel used in thermal power plants. Comments on the sample comparison:

1. Original sample № 1 showed an abnormally high hydrogen mass fraction value. Such values hydrogen were observed at «NPK EPT» in the heating tubes of thermal power plant steam boilers

under the following conditions: steam pressure of 300 atm, internal pipe temperature above 300°C, and accumulation time of ~170,000 hours (24 years).

2. During the forging process, sample № 4 "lost" 31% of its hydrogen content compared to original sample No. 1 due to plastic deformation.

3. The plate (samples № 2 and 3) were preheated, resulting in 88% of the initial hydrogen being extracted into the atmosphere.

It is important to note the ratio between the hydrogen groups extracted at different temperatures: at 530°C, hydrogen with a low binding energy (0.3 to 0.5 eV), known as diffusion-mobile hydrogen (DMH), is extracted; at 800°C, hydrogen with a higher binding energy of ~1 eV, known as strongly bound hydrogen (SBH), is extracted. The ratio of the DMH content to the SBH content was: Sample 1: Q_{DMH}/Q_{SBH} = 3.4. Sample 2: Q_{DMH}/Q_{SBH} = 2.1. Sample 3: Q_{DMH}/Q_{SBH} = 1.7. Sample 4: Q_{DMH}/Q_{SBH} = 4.04.

Conclusions. The chemical composition analysis of the sledgehammer shows that its material is very pure iron with a characteristic spectrum of impurities (Mn, Ni, Co), which is unusual for industrial iron and typical of natural iron. This supports the conclusion that the artifact is not made of meteorite or smelted steel, but of a naturally occurring material—native iron with an anomalously high hydrogen content. This supports V.N. Larin's hypothesis of an initially hydridic Earth (Larin, 1980). This first-ever result on the anomalously high hydrogen content strongly supports this highly controversial hypothesis. This hypothesis attributes a key role in the Earth's evolution to hydrogen, which is released unevenly from the planet's core through the crust during the decay of hydrides. Finds of naturally occurring pure native iron are numerous (Tomshin et al., 2023), but their hydrogen content has not previously been determined. The authors' discovery of the superplasticity of hydrogen-containing iron (a sample can be scratched with an ordinary nail) will facilitate the search and selection of new samples, which is necessary to confirm the anomalously high hydrogen content in a natural sample, which has been rigorously proven for the first time through analytical methods. It is possible that similar finds, previously noted in various parts of the Earth, may be markers of hydrogen deposits, which have recently attracted considerable interest (Glazyev et al., 2023).

Acknowledgments. The authors thank researcher and PhD candidate Yu. A. Yakovlev for analyzing the hydrogen in the archaeological artifact.

Funding. *This work was supported by a state assignment from the Institute of Physics of the Earth, Russian Academy of Sciences.*

References

1. Glazyev S. Yu., Bezrukov L. B., Dolgolaptev A. V., Larin N. V., Syvorotkin V. L., Fedorov V. M. Climate Change and Energy Transition // Economic Strategies. 2023. — No. 6 (192). — P. 16–29.
2. Larin V. N. Hypothesis of a Primordial Hydridic Earth (A New Global Concept) Moscow: Nedra. — 1980. — 216 p.
3. Mezenin N.A. Interesting Facts about Iron. 3rd Edition. Moscow: METALLURGY. — 1985. — 176 p.
4. Nikolaev E.N. Some Issues of Classification of Yakut Bloomery Furnaces // Bulletin of Tomsk State University. — 2021. — №. 465. — P. 124-132.
5. Persikov E.S., Bukhtiyarov P.G., Aranovich L.Ya., Shaposhnikova O.Yu., Nekrasov A.N. Experimental Modeling of the Formation of Native Metals in the Earth's Crust During the Interaction of Hydrogen with Basaltic Melts // Geochemistry. — 2019. — Vol. 64. — №. 10. — P. 1015–1025.
6. Persikov E.S., Bukhtiyarov P.G., Aranovich L.Ya., Shaposhnikova O.Yu., Nekrasov A.N. Experimental modeling of the process of formation of native metals in the earth's crust during the interaction of hydrogen under reducing conditions // Petrology. — 2025. — Vol. 33. — № 5. — P. 5–17.
7. Commercial dictionary, containing knowledge of the goods of all countries, and the names of the main and newest things related to commerce, also to house-building, knowledge of arts, handicrafts, factories, mining, paints, spicy potions, herbs, precious stones, etc. / Translated from French by Vasily Levshin. — Moscow: Type. Comp. printing house. — 1787–1792. — P. 8.
8. Tomshin M.D., Kopylova A.G., Vasilyeva A.E. Native iron in Siberian traps // Petrology. — 2023. — Vol. 31. — №. 2. — P. 202–216
9. Tselmovich V.A., Shelmin V.G., Maxe L.P. Microscopic traces of the 1984 Chulym bolide. // Lithosphere. — 2025. — 25 (4). — P. 961–976.
10. D. Huang, M. Murakami, S. Gerstl et al. Experimental quantification of hydrogen content in the Earth's core //Nat Commun . – 2026. — 17. — 1211. https://doi.org/10.1038/s41467-026-68821-6